UNIVERSIDAD DE CONCEPCIÓN
FACULTAD DE CIENCIAS FÍSICAS Y MATEMÁTICAS

N_2H^+ KINEMATICS IN THE G012.80 PROTOCLUSTER

Evidence for filament rotation and evolution

Por: Javiera C. Salinas

Tesis presentada a la Facultad de Ciencias Físicas y Matemáticas de la Universidad de Concepción para optar al grado académico de Magíster en Astronomía.

Noviembre 2024
Concepción, Chile

Profesor Guía: Amelia M. Stutz

Dedicada a mi familia y amigos.

AGRADECIMIENTOS

Agradezco profundamente a mi familia, quienes han estado conmigo desde el inicio y me han acompañado en cada etapa de mi carrera. En especial, agradezco a Rossana y Jorge, quienes han sido como padres para mí. Gracias por apoyarme en cada paso que doy, por aconsejarme en los períodos difíciles y por estar siempre disponibles para lo que he necesitado. También agradezco a mis hermanos por ser parte de estos momentos tan importantes en mi vida, por quererme y por esa curiosidad que los caracteriza.

Agradezco a mi profesora guía, Amy, quien ha sido una parte esencial de mi formación y de la finalización de este proyecto. Gracias por aconsejarme y preocuparte por mi desarrollo como investigadora. También agradezco a mis compañeros y amigos del grupo de formación estelar, Rodrigo y Nico, por su buena disposición y por la retroalimentación que brindaron para este proyecto.

Agradezco a mis amigos, quienes me han acompañado en los momentos más difíciles durante mi período de magíster y han sabido ser incondicionales conmigo. Gracias por regalarme tantas risas y momentos inolvidables. A mis amigos de la academia, agradezco haber coincidido en este camino; espero que, dentro de muchos años, sigamos construyendo esta bonita amistad. Aunque tomemos diferentes caminos, deseo de todo corazón que logren todo aquello que anhelan y que siempre permanezcamos en contacto.

Agradezco a mi novio por ser un apoyo fundamental en estos últimos años. Gracias por tu amor y por impulsarme a alcanzar todo lo que quiero. También agradezco a tu familia por abrirme las puertas de su hogar, por quererme y por ser como una segunda familia aquí en Concepción.

Asimismo, agradezco a aquellos que ya no están. En especial, a mi hermano. Gracias, Samu, por las inolvidables pláticas sobre el universo que siempre atesoraré en mi corazón. Gracias por ser un conciliador en mi vida.

Finalmente, me agradezco a mí misma: una mujer resiliente, valiente e inteligente, que siempre persigue aquello que la motiva.

Resumen

Nuestro principal objetivo es caracterizar la cinemática del gas denso a través de la molécula de N_2H^+ en el protocúmulo G012.80. Para complementar los datos de N_2H^+, empleamos observaciones de DCN, SiO, H41α, $C^{18}O$ y mapas de continuo. Todas las observaciones provienen del proyecto ALMA-IMF.

Analizamos múltiples componentes de velocidad mediante el ajuste hiperfino de N_2H^+, encontrando que dos componentes principales dominan la región. Estimamos gradientes de velocidad en dos de los filamentos principales (R1 y R2), los cuales trazan diferentes estructuras en diagramas posición-velocidad (PV). Utilizando los parámetros obtenidos del ajuste hiperfino de N_2H^+, estimamos la columna de densidad, las masas y los perfiles de masa. Los diagramas PV muestran estructuras en zigzag, enroscadas y helicoidales en el gas denso. En los dos filamentos principales, observamos diferencias significativas en las estructuras PV. En el filamento R1, se identifican estructuras helicoidales potencialmente asociadas con la rotación del filamento, además de una baja cantidad de cores. En contraste, R2 muestra estructuras oscilantes distribuidas en un rango de velocidad más estrecho, probablemente relacionadas con el colapso de cores masivos. En el filamento R1 identificamos un gradiente perpendicular asociado con una escala de tiempo de $\sim 0.1\,\mathrm{Myr}$, mientras que R2 no presenta gradientes de velocidad claros.

Los perfiles de masa en ambos filamentos se describen adecuadamente mediante las funciones $\lambda(\omega) = 5660\,(\omega/\mathrm{pc})^{0.30}$ para R1 y $\lambda(\omega) = 6943\,(\omega/\mathrm{pc})^{0.20}$ para R2. El filamento R2 tiene una tasa de formación estelar (SFR) de $55.3\,\mathrm{M}_\odot$ Myr^{-1} y una eficiencia de formación estelar similar a la observada en el filamento ISF de Orión. Por otro lado, el filamento R1 solo contiene cores clasificados como prestelares, los cuales son menos masivos que los de R2. Considerando las diferencias cinemáticas, las tasas de formación estelar y los perfiles de masa en ambos filamentos, proponemos que R1 aún está rotando y representa una etapa más temprana de evolución, mientras que R2 ha colapsado más significativamente, alcanzando un estado más eficiente de formación estelar. Por tanto, G012 alberga filamentos masivos en diferentes etapas evolutivas.

Keywords – ISM: nubes - ISM: cinemática y dinámica - ISM: moléculas - ISM: regiones H II - ISM: evolución

Abstract

We aim to characterize kinematic processes in the G012.80 protocluster (hereafter G012), also known as the W33 main clump. We principally use N_2H^+ (1−0) emission to trace the dense and cold gas in G012. Additionally, we reviewed complementary spectral lines including DCN, H41α, $C^{18}O$, SiO, and continuum maps, all observations were provided by the ALMA-IMF Large Program.

We perform a N_2H^+ hyperfine spectral line fitting to analyze multiple velocity components and extract spectral parameters. We estimated velocity gradients, column densities, and line-mass profiles for the two main filaments, R1 & R2, which show distinct position-velocity (PV) features. In the PV diagrams we observe zig-zag, twisting, and turning velocity structures pervasively in the dense gas. However, R1 exhibits a gradient feature of $10.4\,\mathrm{km\,s^{-1}\,pc^{-1}}$, corresponding to an estimated timescale of 0.1 Myr, potentially associated with filament rotation, as well as few cores above the completeness limit. In contrast, R2 exhibits compact velocity structures ($\Delta V \sim 3\,\mathrm{km\,s^{-1}}$), likely related to collapse, as evidenced by the presence of a comparatively large number of massive cores.

Line-mass profiles follow $\lambda(\omega) = 5660\,(\omega/\mathrm{pc})^{0.30}$ for R1 and $\lambda(\omega) = 6943\,(\omega/\mathrm{pc})^{0.20}$ for R2, where ω is the projected radius in the plane-of-the-sky of the aligned filaments. R2 forms prestellar and protostellar cores at a star formation rate of $\mathrm{SFR} = 55.3\,\mathrm{M_\odot\,Myr^{-1}}$, with efficiency similar to Orion ISF. In contrast, the R1 filament, which lacks protostellar cores, only contains a few cores in the prestellar phase, resulting in an SFR of $4.24\,\mathrm{M_\odot\,Myr^{-1}}$. Considering the dense gas kinematic, core formation, and line-mass profiles difference, we propose that R1 is still rotating and younger than the R2 filament, which has evolved further, toward collapse, to a higher star formation rate. G012 thus contains massive filaments in different evolutionary stages.

Keywords – ISM: clouds - ISM: kinematics and dynamics - ISM: molecules - ISM: H II regions - ISM: evolution

Contents

List of Tables

List of Figures

Chapter 1

Introduction

Protoclusters, or embedded clusters, are gas-dominated regions where stars are actively forming. Unlike clusters where gravity is dominated by the stars themselves, protoclusters are defined by the gravitational influence of the dense gas from which the stars emerge (Stutz, 2018). Studying these regions is crucial for understanding the early stages of star formation, particularly the formation of high-mass stars, which significantly impact their surroundings through outflows, radiation, and supernovae (Motte et al., 2018). These massive stars play a vital role in shaping the evolution of galaxies and in estimating star formation rates across the universe, making the study of protoclusters and the processes within them essential for understanding key astrophysical phenomena. In this context we have filaments, elongated and dense gas structures that are the birth sites of prestellar and protostellar cores. These filaments can be detected at scales of molecular clouds but also at small protocluster-scales. Thus, filaments are the immediate gas reservoir from which the cores are accreting (e.g., Kirk et al., 2013; Stutz and Gould, 2016; Stutz et al., 2018; Williams, 2018; Zhou et al., 2022; Hacar et al., 2023; Louvet et al., 2024).

To gain a deeper insight into high-mass star formation (HMSF), it is essential to examine the physical conditions and kinematic properties of the molecular gas. Key parameters to understand molecular HMSF include gas density, temperature, and the kinematic distributions that can be derived from molecular spectra emitted by different tracers. The analysis of these measurements allow us to develop further constraints of processes taking place in HMSF environments, such as gas infall,

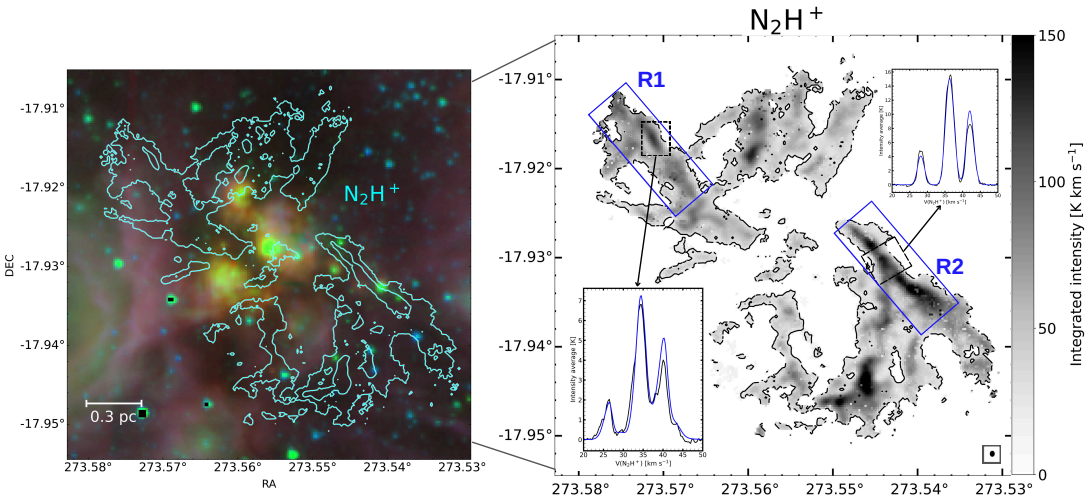

Figure 1.0.1: Left panel: Spitzer RGB composite figure of the G012 protocluster at 8 μm (red), 4.5 μm (green) and 3.6 μm (blue). Cyan contour shows the N_2H^+ integrated intensity emission at 25 and 100 K km s^{-1}. Right panel: N_2H^+ integrated intensity map. Black contour shows emission at 25 K km s^{-1}, considering a $S/N > 12$. Blue boxes highlight two main filamentary structures, R1 & R2, with estimated lengths of 0.56 pc for both (see text). We show the representative spectra of both regions in the insets: the black curve represents the data, and the blue curve is the N_2H^+ data modeled with one velocity component. The integrated intensity shows a "disrupted" morphology, with filamentary structures around the protocluster's center. The black ellipse in the bottom-right corner represents the beam size of the N_2H^+ data.

outflows, ionizing radiation, and filament rotation (e.g., Galván-Madrid et al., 2010; Kong et al., 2019; González Lobos and Stutz, 2019; Álvarez-Gutiérrez et al., 2021; Motte et al., 2022; Ginsburg et al., 2022a; Cunningham et al., 2023; Liu et al., 2023; Galván-Madrid et al., 2024; Armante et al., 2024; Álvarez-Gutiérrez et al., 2024; Dell'Ova et al., 2024; Louvet et al., 2024; Sandoval-Garrido et al., 2024; Towner et al., 2024). Turning to the dense and cold gas, one of the main tracers is diazenylium, most commonly recognized as N_2H^+ (e.g., Bergin and Langer, 1997; Caselli et al., 1995; Bergin and Tafalla, 2007; Lippok et al., 2013; Tatematsu et al., 2008; Busquet et al., 2011; Gómez et al., 2022). The Nitrogen-bearing molecule is characterized by lower depletion onto dust grains at low temperatures, and was first detected in the interstellar medium (ISM) by Thaddeus and Turner (1975).

Previously, Tobin et al. (2013) estimated abundances of N_2H^+ and N_2D^+ molecules in protostellar systems. One of these systems (L1157) reveals that $C^{18}O$ traces regions lacking N_2H^+. They find that as the $C^{18}O$ peaks decrease, N_2H^+ increases,

demonstrating a clear anticorrelation between the abundances of both tracers. This anticorrelation is also detected by Tafalla et al. (2021), where they also show that N_2H^+ is detected at high column densities ($N(H_2) \geq 10^{22}\,cm^{-2}$; see their Fig. 7). In addition, Yu et al. (2022) analyzed a H II bubble (S156) associated with the G305 star forming complex, finding that N_2H^+ increases far to the edges of S156. This implies that N_2H^+ is actually destroyed by the hot gas in the bubble. As well as increased CO near H II regions, free electrons traced by recombination lines (e.g., H41α), ionized metal emission lines, and continuum emission provide additional methods to map these zones where N_2H^+ is destroyed (e.g., Yu et al., 2018; Ginsburg et al., 2022a; Galván-Madrid et al., 2024; Armante et al., 2024). Galván-Madrid et al. (2024) analyzed the 3 mm continuum emission and H41α recombination line data for the full ALMA-IMF sample, finding that an increase in emission is mostly seen in evolved regions where OB associations exist. All of these studies, along with the effect of temperature on the critical density of the N_2H^+ molecule (ranging from $6.1 \times 10^4\,cm^{-3}$ at 10 K to $2.0 \times 10^4\,cm^{-3}$ at 100 K), suggest a close relationship between the decrease in N_2H^+ and the evolutionary stages of the protocluster. The critical density indicates the conditions under which N_2H^+ becomes an effective tracer, thus linking its observed decrease to changes in the protocluster condition.

Indeed, taken in aggregate various mm-wave observables, such as the continuum emission levels compared to the H41α emission, are presently being used to establish evolutionary stages of protocluster samples across the Milky Way (e.g., Motte et al., 2022; Galván-Madrid et al., 2024). However, when the kinematics and dense gas emission are scrutinized in individual protoclusters, we see the emergence of a scenario pointing toward multiple evolutionary stages (or multiple generations or episodes of star formation) inside a given protocluster, as shown in Cunningham et al. (2023). This situation drives the need for scrutiny of “evolved" protoclusters with internal structures at (potentially) different evolutionary stages. Moreover, the search for correlations in the kinematic properties of these dense-gas structures (e.g., Stutz and Gould, 2016; Xu et al., 2023; Álvarez-Gutiérrez et al., 2024; Sandoval-Garrido et al., 2024) with evolutionary stage and the mass profiles (or in the case of filaments the line-mass profiles, e.g., Stutz, 2018), sets the stage for the development of observationally-driven physical models and interpretations of the internal evolution of protoclusters, as the stellar mass is being assembled.

In this context, here we predominantly focus on the ALMA-IMF protocluster G012 and its two dominant internal cold dense gas structures identified with diazenylium. These structures have the form of coherent filaments that show evidence for either rotation or collapse.

G012 is one of the 15 nearby massive protoclusters observed by the ALMA-IMF Large Program (LP). ALMA-IMF aims to infer the origin of the initial mass function (IMF) in our galaxy, as well as providing an unprecedented variety of data from different structures inside the full sample (Motte et al., 2022). This LP focuses on a variety of separate but related topics and techniques, such as the analysis of the different populations of cores in the sample (e.g., Cunningham et al., 2023; Pouteau et al., 2022, 2023; Nony et al., 2023; Louvet et al., 2024, Motte et al. accepted), detection of organic molecules (e.g., Bonfand et al., 2024; Armante et al., 2024), study of outflows (e.g., Towner et al., 2024), and also (but not exclusively) gas kinematics and large-scale structures (e.g., Álvarez-Gutiérrez et al., 2024; Sandoval-Garrido et al., 2024).

Specifically, G012 is an active and massive ($4.6 \times 10^3\,M_\odot$, see Motte et al., 2022) star-forming region centered on the W33 main clump, with an estimated distance of 2.4 kpc (Immer et al., 2013) and a local standard of rest velocity of $V_{lsr} = 37\,km\,s^{-1}$, as estimated through maser velocities in Immer et al. (2014). Previously, Immer et al. (2013) reported the presence of a star cluster in the G012 center with spectral types from O7.5 to B1.5, in addition to dissociation of complex molecules due to interaction with CO molecule on small scales (e.g., Immer et al., 2014). Given its evolutionary state, detections of HC_3N, CO outflows, class I methanol masers, presence of H II regions, OB star clusters, and high abundance of cores, G012 is an optimal testbed for studying mechanisms affecting dense gas, filament kinematics, and HMSF in the region (e.g., Haschick and Ho, 1983; Yu et al., 2019; Xie et al., 2023; Armante et al., 2024).

To explore the dense gas kinematics traced by N_2H^+ in the G012 protocluster, we analyze several key aspects. These include moment maps, position-velocity (PV) diagrams, and average-velocity gradients. Additionally, we estimate the column density, line-mass profiles, and the star formation rate (SFR) and star formation efficiency (SFE) of the two main filaments in G012 (R1 and R2; see below and Fig. 1.0.1). We found that R1 & R2 filaments present different and intricate features in PV diagrams. R1 shows rotation signatures, while R2 exhibits

kinematics mostly influenced by the massive cores within the filament. We propose that the variations between the R1 and R2 filaments could be attributed to different stages of evolution. While one filament hosts more cores and forms them with an efficiency comparable to the Integral Shaped Filament in Orion (ISF), the other main filament remains in an earlier and rotating stage, exhibiting behavior similar to that observed in the California L1482-S molecular cloud (e.g., Álvarez-Gutiérrez et al., 2021).

This paper is organized as follows. In Sec. 2 we detail the ALMA-IMF dataset and cores catalogs for the G012 protocluster. In Sec. 3 we analyze the N_2H^+ moment maps, PV diagrams, core velocities, and column density in the region. We perform a detailed analysis of the two dominant cold dense gas structures in Sec. 4, focusing on average-velocity gradients and line-mass profiles in the R1 & R2 filaments. In Sec. 5, we compare the observed rotation in the R1 filament with the filament mass. Finally, we discuss about a potential different evolutionary scenario in the region and summarize our main conclusions in Sec. 6 and Sec. 7, respectively.

Chapter 2

Data

In this section we describe the ALMA data set and catalogs used in this paper. We use G012 protocluster observations from the Atacama Large Millimeter Array (ALMA) telescope provided by the ALMA-IMF Large Program , project # 2017.1.01355.L. Basic parameters of the G012 protocluster are presented in Table 2.0.1, while the most fundamental line parameters for N_2H^+ and additional tracers are summarized in Table 2.2.1.

Table 2.0.1: Center coordinates, velocity, and key parameters of the G012.80 protocluster

RA [IRCS]	DEC	V_{lsr}[a] [km s^{-1}]	d [kpc]	$Mass_{870\mu m}$ [$\times 10^3$ M$_\odot$]	Size (B6 | B3)[b] [pc × pc]	Evolutionary[c] stage
18:14:13.37	-17:55:45.2	+35.5	2.4 ± 0.2	1.7	1.5 × 1.5 | 2.2 × 2.1	Evolved

(a) V_{lsr} estimated through N_2H^+ centroid velocities. (b) Physical areas of primary beams in band 6 and band 3. (c) Evolutionary stage calculated from 1.3 mm to 3 mm flux ratio and free-free emission flux density (Motte et al., 2022; Galván-Madrid et al., 2024).

2.1 ALMA-IMF datacubes

We mainly employ N_2H^+ (J=1−0) observations at a frequency of 93.1734 GHz. We follow a similar N_2H^+ data reduction prodecure as Álvarez-Gutiérrez et al. (2024) and Sandoval-Garrido et al. (2024). We briefly described the procedure steps below.

To recover the cloud emission at all available scales, we combine observations of the 7 m and 12 m arrays with total power data (TP). N_2H^+ observations were cleaned using ALMA-IMF imaging pipeline[1] and the version 5.6.0 of *The Common*

Astronomy Software Applications package (CASA). We use the imcontsub task to subtract the continuum emission from the N_2H^+ line emission. To estimate the continuum emission we consider only emission-free channels and being described as constant across the N_2H^+ cube (fitorder = 0). We use the *feather* task to re-sample and combined and combine the 7 m+12 m imaging with the TP observations. This combination allowed us to recover the missing flux, visible as negative bowls in the interferometric data. From the procedure described above we obtain a fully integrated, multi-scale emission dataset. These data will be published by Stutz et al. (in prep). The resulting N_2H^+ data cube contains a total of 217 velocity channels over a range from 12 km s^{-1} to 61 km s^{-1}, with a velocity resolution of 0.23 km s^{-1}. The final beam size is given by $2.59'' \times 2.1''$ (major beam × minor beam) with an associated beam position angle (BPA) of 89.3 °.

In Fig. 1.0.1 we display Spitzer observations at 8 μm (red), 4.5 μm (green) and 3.6 μm (blue) along with an N_2H^+ integrated intensity contour at 50 K km s^{-1} (left panel) and N_2H^+ integrated intensity map at signal-to-noise ratio $(S/N) > 12$ (right panel). In the N_2H^+ integrated intensity map, G012 is characterized by the presence of a swirling and filamentary distribution (see also Figure 2.1.1) in the plane-of-the-sky (POS). Specifically, we highlight the two prominent filaments with blue boxes, which are the focus of this study, hereafter called R1 & R2 (and see below).

Aside from the N_2H^+ data, we also use the H41α, DCN, SiO, and $C^{18}O$ spectral lines, as well as the continuum emission at 3 mm (band 3, centered at a frequency of 99.66 GHz) and 1.3 mm (band 6, centered at 230.6 GHz); both maps have fields of view (FOV) of $190'' \times 180''$ and $132'' \times 132''$ for band 3 and 6 (Ginsburg et al., 2022a), respectively. As G012 is an evolved region, we use the H41α recombination line (Cunningham et al., 2023; Galván-Madrid et al., 2024) at a velocity resolution of 1.8 km s^{-1}. This traces free-free radiation of H II regions at high temperatures (> 100 K) related to evolved star associations in the protocluster center. In addition, we analyze outflows features through the SiO (J=5−4) line emission at a velocity resolution of 0.39 km s^{-1} (Cunningham et al., 2023; Towner et al., 2024). We complement the N_2H^+ dense gas emission using DCN (J=3-2), which traces more compact and hotter emission compared to N_2H^+. Finally, we use $C^{18}O$ (J=2-1) emission at a velocity resolution of 0.33 km s^{-1} (Koley et al. in prep).

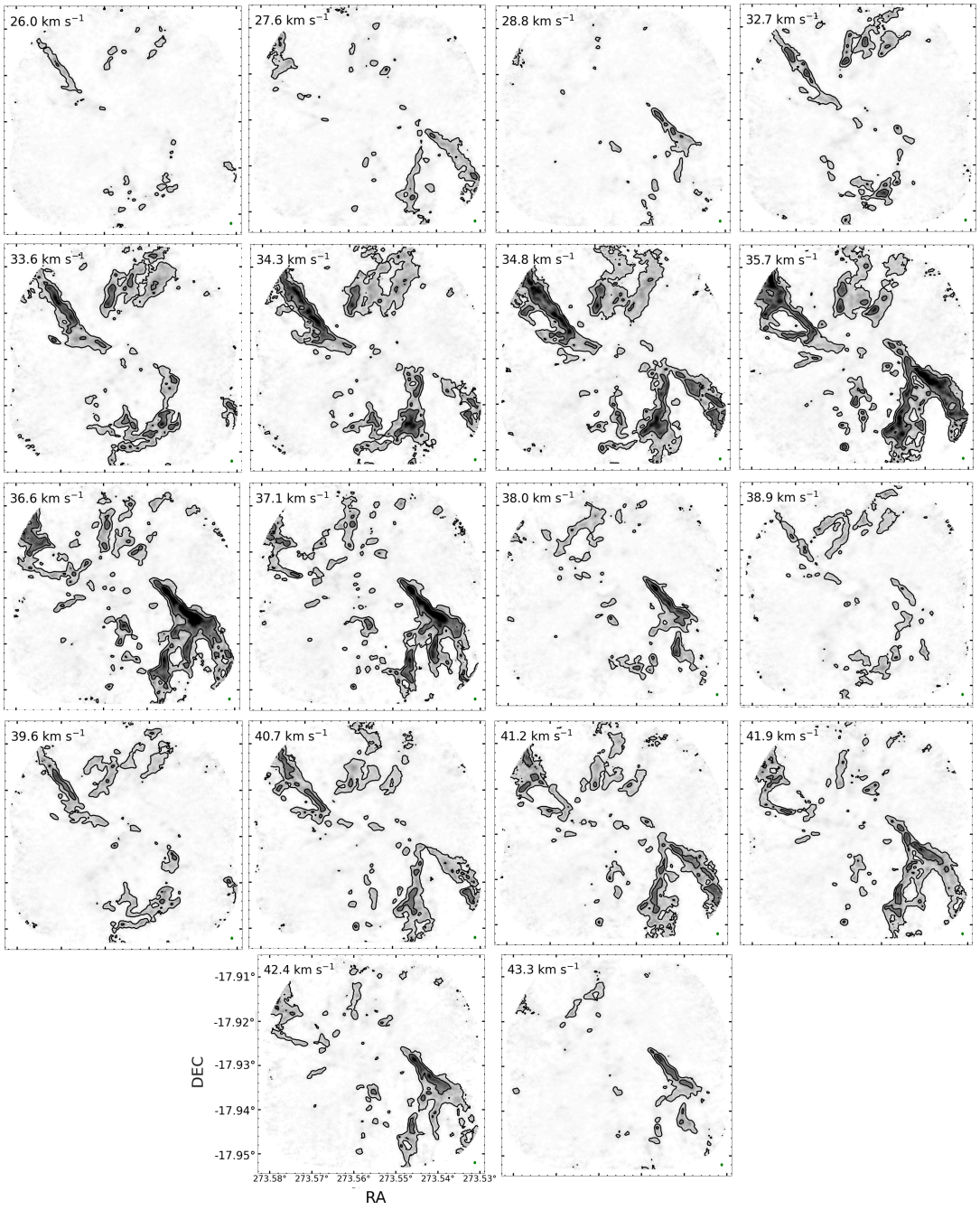

Figure 2.1.1: N_2H^+ intensity maps at different velocity channels (velocities are indicated in the upper-left of each panel). Contour levels highlight structures enclosing intensities at 4 K (outer level), 10 K (middle level) and 20 K (inner level). More intense and well-defined structures appear between velocities of 34 km s^{-1} to 37 km s^{-1}, in agreement with the range in which the velocity centers are distributed.

2.2 ALMA-IMF core catalogs

Louvet et al. (2024) constructed the first core catalog of the full ALMA-IMF sample based on the 1.3 mm and 3 mm continuum data. To extract and identify compact emission, they used *Getsf* and *GExt2D* toolkits. In G012, they found a total of 66 cores with respective mass and size estimates. As followup, Cunningham et al. (2023) used the DCN line emission to study the core population from Louvet et al. (2024). For G012, they were able to estimate spectral parameters of 36 cores, including their radial velocities. Recently, Armante et al. (2024, hereafter A24) constructed a G012 catalog of prestellar, protostellar, and hot cores detected with dust continuum emission (at both 1.3 mm and 3 mm), ^{12}CO (2-1), SiO (5-4), CH_3OCHO and CH_3CN spectral lines. A24 found a total of 101 cores with mass and size estimates, within the sources of the continuum (Louvet et al., 2024). Additionally, Motte et al. (2024, accepted) re-estimate the masses for the A24 sample of cores, and provide new mass estimates for cores in the remaining ALMA-IMF protoclusters, using radiative transfer methods. To complement the datacubes mentioned above and to provide a more complete characterization of the G012, we make use of the core catalogs described above in our analyses.

Table 2.2.1: Spectral line set-up

1

Line	Frequency [GHz]	Velocity resolution [km s^{-1}]	BMAJ^a [″]	BMIN^b [″]	BPA^c [°]	S/N^d
N_2H^+ (*)	93.174	0.23	2.59	2.10	89.3	12
DCN	217.15	0.39	1.29	0.88	76.0	5
H41α	92.200	1.8	2.28	1.93	84.9	7
C^{18}O	219.56	0.33	1.33	0.90	77.4	5
SiO	217.15	0.39	1.29	0.88	77.0	5

(a) Major beam. (b) Minor beam. (c) Beam position angle. (d) Signal-to-noise ratio cut applied for the analysis. (*) The only tracer that includes total power data. All others only considered 7 m and/or 12 m arrays.

Chapter 3

Data analysis

To determine key kinematic parameters based on the full N_2H^+ hyperfine line complex, we model the N_2H^+ data cube. This will also permit the identification of multiple velocity components in a given spectrum. We adopte a similar fitting procedure as Sandoval-Garrido et al. (2024) to model the N_2H^+ emission of the spectra in the data cube. We use the hyperfine line structure model provided by version V.1.0.1 of `PySpecKit` spectroscopic analysis toolkit (Ginsburg et al., 2022b). We applied a fitting model for two velocity components, using parameters such as excitation temperature (T_{ex}), optical depth (τ), velocity centroid (V_c), and velocity dispersion (σ). The resulting fits reveal that G012 is characterized by two velocity components, allowing us to define two primary velocity structures: the first velocity component (FVC) and the second velocity component (SVC). These components are separated by a velocity boundary at 35.6 km s^{-1}, calculated from the overall velocity distribution (see Appendix A1). In what follows, FVC refers to spectra associated with velocities smaller than this boundary, while SVC refers to those spectra above it, guiding our velocity components identification. In Appendix A1, we describe the data preparation steps and N_2H^+ line fitting, including a S/N analysis to select reliable values and determine the spectral fitting input parameters. We also describe the line fitting of the complementary tracers mention above and list in Table 2.2.1.

Using the FVC and SVC structures, we further explore the kinematics of G012 through several complementary analyses. First, we review moment maps that provide a detailed look at the velocity centroid and dispersion patterns across the

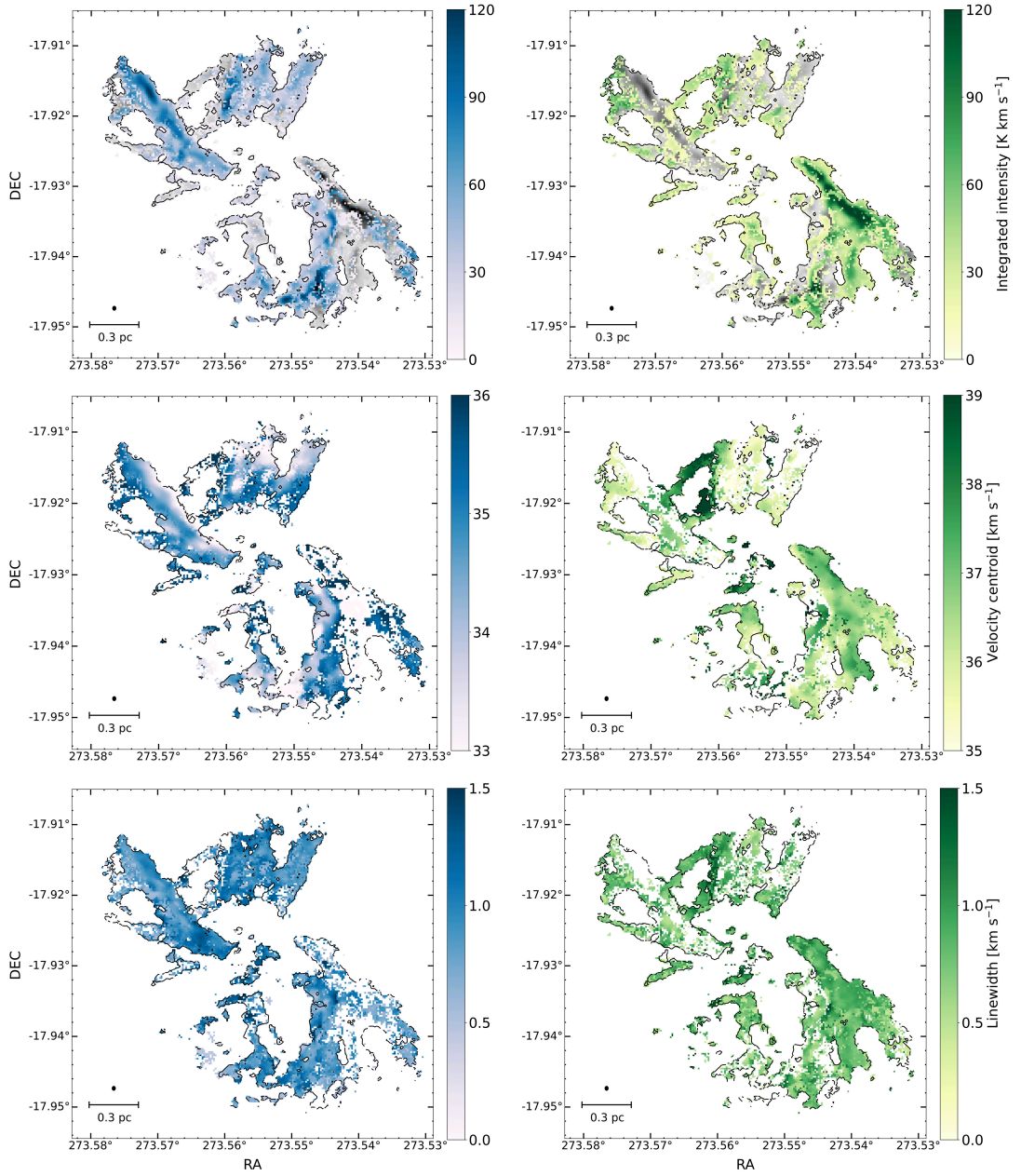

Figure 3.0.1: Integrated intensity (upper panels), velocity centroid (middle panels), and velocity dispersion (bottom panels) of the FVC (left panels, blue) and SVC (right panels, green). Black contours are the same showed in Figure 1.0.1. The grey background in upper panels represent the total integrated intensity in order to contrast the spatial distribution of both velocity components. Black boxes in the upper panels display the spatial location of the R1 and R2 filaments. The black ellipse at the bottom-left corner represents the beam size of the N_2H^+ data.

region. We then construct PV diagrams of the entire region to capture the velocity

gradients and dynamical behavior of the protocluster. We also estimate column densities and masses in G012 in order to set constraints on the gas distribution and density profiles in the region.

3.1 Moment maps

In Fig. 3.0.1, we display the N_2H^+ integrated intensity (upper panels), velocity center (middle panels), and velocity dispersion (bottom panels) maps for the FVC and SVC. We observe two dense and prominent filaments in the N_2H^+ data that are dominated by different velocity structures. The R1 filament is primarily associated with the FVC, while R2 is mainly associated with the SVC. The FVC kinematics shows gradient structures in R1, with a mean velocity difference of $\sim 3\,\mathrm{km\,s^{-1}}$. The mean values of the centroid velocities and velocity dispersion for the R1 filament are of $\langle V \rangle = 34.4\,\mathrm{km\,s^{-1}}$ and $\langle \sigma \rangle = 0.81\,\mathrm{km\,s^{-1}}$, respectively. In contrast, the SVC exhibits more homogeneous structures in velocity. The mean values of the SVC centroid velocities and velocity dispersion maps are of $\langle V \rangle = 36.8\,\mathrm{km\,s^{-1}}$ and $\langle \sigma \rangle = 0.75\,\mathrm{km\,s^{-1}}$, respectively.

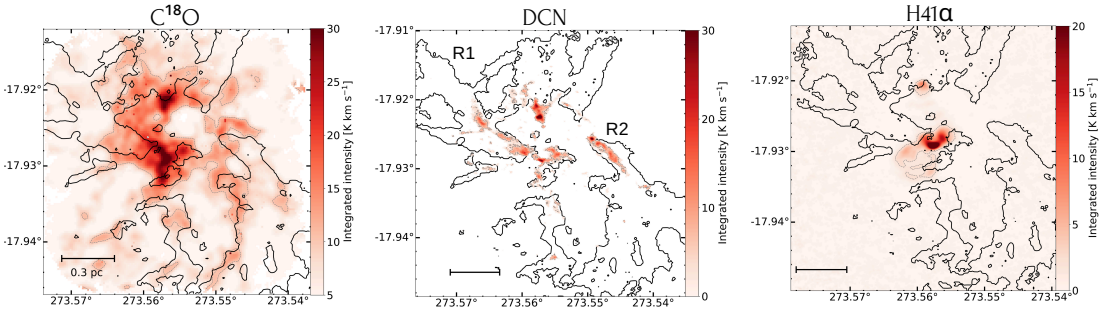

Figure 3.1.1: Integrated intensity of the complementary tracers: $C^{18}O$ (left panel), DCN (middle panel), and H41α (right panel). The black contour shows N_2H^+ integrated intensity at $50\,\mathrm{K\,km\,s^{-1}}$, and the scale-bar indicates 0.3 pc at the distance of G012. Gray contours are at integrated intensity values of 3, 5, and $10\,\mathrm{K\,km\,s^{-1}}$ for DCN, H41α, and $C^{18}O$, respectively. The H41α recombination line and $C^{18}O$ emission are mostly concentrated at the center of G012, where N_2H^+ is mostly abscent and an OB type stars cluster is located. In the areas surrounding the R1 and R2 filaments, we observe a distribution of lower $C^{18}O$ integrated intensity emission. DCN traces some regions of the main N_2H^+ structures, and its emission is associated with cores and filaments. Specifically, DCN dominates the top of the R2 filament, central regions of the protocluster, at the edges of R1, and surroundings of the H41α bubbles.

Additionally, at the center of G012 we observe an absence of N_2H^+ emission that

may be related to the destruction of the molecule in the region. Two chemical processes can lead to the dissociation of the N_2H^+ molecule: photodissociation through interactions with CO (Bergin and Langer, 1997; Caselli et al., 2002; Caselli and Ceccarelli, 2012) and dissociative recombination with free electrons (Vigren et al., 2012).

To analyze the absence of N_2H^+, we review the integrated intensity maps of the fitted complementary tracers and the continuum emission. We observe that the 1.3 mm continuum emission is concentrated at the center of G012 and to the north of R2. Moreover, the 3 mm continuum exhibits high-flux intensity distributions appearing as bubbles in the protocluster center (Ginsburg et al., 2022a), similar to the H41α distribution (right panel of Fig. 3.1.1). The $C^{18}O$ emission traces more extensive gas than N_2H^+ and is primarily distributed around the H41α bubbles (left panel of Fig. 3.1.1). We also observe high $C^{18}O$ integrated intensity structures in the surroundings of R1 & R2. Given the high concentrations of H41α and $C^{18}O$ in the center of G012, it is likely that the central H II region is destroying the N_2H^+ emission through interactions with free-free electrons and CO. On the other hand, DCN traces some dense parts of the filamentary structures in R1 & R2 (middle panel of Fig. 3.1.1). In addition, SiO integrated intensity reveals elongated features in the R2 filament (see Fig. 3 in Armante et al., 2024). Specifically, is observed one perpendicular feature at the top of R2 related to a previous detected hot core.

3.2 N_2H^+ PV diagrams

We use the technique developed in González Lobos and Stutz (2019) to construct the N_2H^+ intensity-weighted position velocity diagrams (e.g., Álvarez-Gutiérrez et al., 2021, 2024; Sandoval-Garrido et al., 2024). In order to avoid projection effects and obtain better defined structures in PV space, we spatially rotate N_2H^+ integrated intensity and velocity center maps by aligning the most predominant filaments (R1 & R2, see upper-left panel in Fig. 3.2.1).

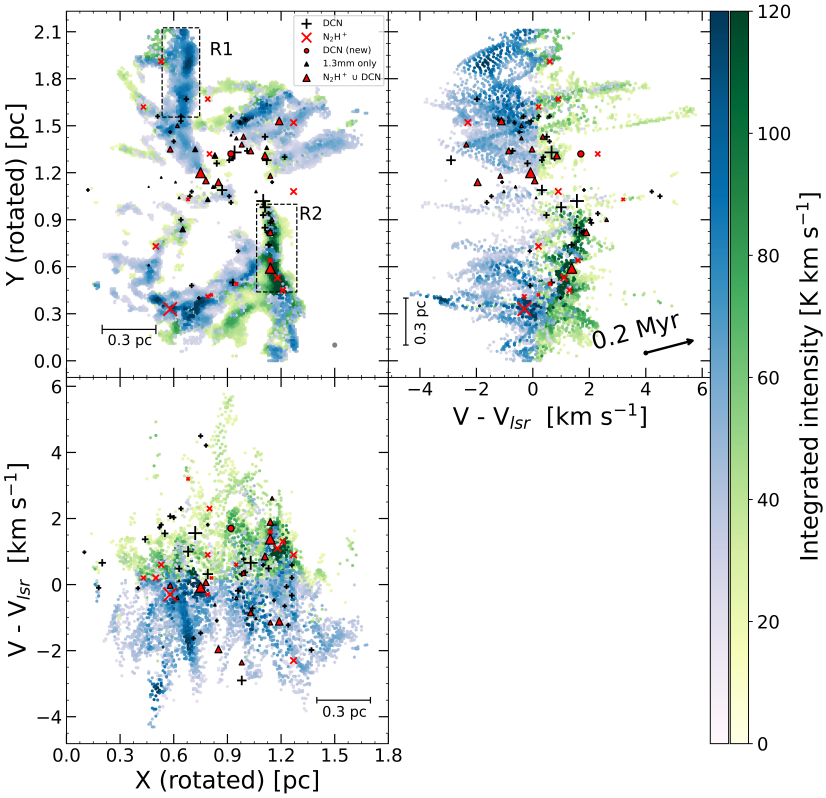

Figure 3.2.1: Position-position and position-velocity diagrams of the N_2H^+ observations. Upper-left: G012 integrated intensity of FVC (blue shades) and SVC (green shades). We display the Cunningham et al. (2023) catalog with black "+" symbols. The Armante et al. (2024) core catalog is divided into four categories: cores detected only with N_2H^+ (red "×" symbols), cores detected only with DCN data (red circles), cores detected with N_2H^+ and DCN (red triangles), and cores not detected in both N_2H^+ and DCN (black triangles). Symbol sizes are proportional to the estimated core mass. The black ellipse in the bottom right corner represents the beam size of N_2H^+. Upper-right: PV diagram along the y-axis; the velocity axis has the V_{lsr} of the protocluster (35.5 km s^{-1}) subtracted. The black arrow illustrates a slope of 5 pc (km s^{-1})$^{-1}$, which corresponds to a timescale of 0.2 Myr. That is, the timescales that approximately correspond to some of the extended structures in this PV diagram. At the top of R1 we observe a wrapped (or "double helix") type velocity field with spreads of more than $\sim$3 km s^{-1}. Meanwhile, R2 appears very compact in velocity along its extent, with small-scale spatial "wiggles". Bottom-left: PV diagram in the perpendicular direction compared to the upper-right panel. Here we observe the emergence, albeit somewhat hidden in the overall velocity field (but see text) of an approximately uniform and extended gradient in R1 apparent near X $\sim$ 0.9 pc, V $\sim$ −1 km s^{-1}. Meanwhile R2 appears as the compact "blob" of cores (triangles and x-symbols) on the r.h.s. of the panel, characterized by the absence of an obvious gradient in position and velocity.

The key features in the PV diagrams are:

1. R1 & R2 main filaments reveal the most predominant and intricate PV structures.
2. R1 filament exhibits a “double-helix" feature. This kind of feature has been associated with filament rotation (e.g., Álvarez-Gutiérrez et al., 2021), a point that we address below.
3. R2 reveals twisting features with a more compact velocity distribution than R1.
4. The PV features are more spread out (short associated timescales) in regions near H41α and SiO emission. This potentially highlights the effect of stellar feedback on the dense gas.

In Fig. 3.2.1 we show PV diagrams of FVC (blue shades) and SVC (green shades) structures. The upper-left panel shows the integrated intesity map after spatial alignment. In the upper-right and bottom-left panels we display the PV diagrams perpendicular and parallel, respectively, to the R1 & R2 regions. Additionally, We include previous cores detected in G012 (Cunningham et al., 2023; Louvet et al., 2024; Armante et al., 2024, Motte et al. accepted). For the PV diagrams, we show a representative timescale of 0.2 Myr related to the PV structures more spread in velocity. In addition to the main features above,we also hilghlight one elongated and high integrated intensity structure in the bottom-left diagram potentially related to the R1 filament.

3.3 Column density and mass

Column density and mass in protoclusters provide insights into the amount of material available for star formation, allowing us to assess the efficiency of the star formation process within the region. Furthermore, understanding the mass distribution helps to elucidate the gravitational influences shaping the evolution of the region, offering a clear picture on how molecular gas accumulates and evolves over time. In order to estimate the N_2H^+ column density, we use the T_{ex}, τ, and σ `PySpecKit` output parameters (see Appendix A1). We apply the column density approximation outlined in Caselli et al. (2002), which is described as follows:

$$N(\mathrm{N_2H^+}) = \frac{4\pi^{3/2} \cdot \nu^3 \cdot Q \cdot \sigma \cdot \tau \cdot \mathrm{e}^{(4.47 \cdot T_{\mathrm{ex}}^{-1})}}{\sqrt{\log(2)} \cdot c^3 \cdot A \cdot g \cdot \left(\mathrm{e}^{\left(\frac{h \cdot \nu}{k \cdot T_{\mathrm{ex}}}\right)} - 1\right)}. \tag{3.3.1}$$

Here, ν represents frequency of the N_2H^+ (1−0) emission, Q is the statistical weight, c is the light speed, A is the Einstein coefficient, E_u corresponds to the upper limit energy of the transition, k_b is the Boltzmann constant, and h is the Planck constant. We extract the spectroscopic constants Q, A, and E_u from Shirley (2015) and Redaelli et al. (2019).

As we reported in Appendix A1, when `PySpecKit` fits optically thin pixels (τ « 1), the T_{ex} parameter automatically adopts its available upper limit (with T_{ex} errors equal to zero) or unusually constant values in specific regions, leading to anomalies in its distribution. To mitigate potential biases introduced by poorly defined values and prevent anomalies in the column density estimates, we excluded all pixels influenced by the τ and T_{ex} estimations. Specifically, we removed pixels where $T_{ex} = 150$ (the fitting upper-limit) and $\tau < 0.2$, discarding 30% of the pixels due to outliers. We then consider the final column density map as the sum of the FVC and the SVC column densities.

The R1 column density map displays similar values to R2, but we observe small differences in their column density distributions. Overall, the R1 overdensities appear more interconnected, compact, and filamentary. Meanwhile, the R2 column density values are distributed more homogeneously, taking high values of around $1 \times 10^{14}\,\mathrm{cm^{-2}}$ in most of the region. We convert N_2H^+ column density to mass units as follows:

$$M(N_2H^+) = N(N_2H^+) \cdot m_{N_2H^+} \cdot A_{pix}. \tag{3.3.2}$$

Here, $m_{N_2H^+}$ and A_{pix} represents the N_2H^+ molecule mass and the pixel area, respectively. The total N_2H^+ mass in the entire protocluster is of $1.72 \times 10^{-5}\,\mathrm{M_\odot}$. Both main filaments, R1 and R2, contribute approximately in a 12% and 17% to the protocluster mass, respectively.

3.4 Relative abundance

Estimating line-mass profiles in filamentary structures (Sec. 4.2) is imperative for capturing their physical conditions, and specifically the effects of gravity. Thus it is the starting point for any filamentary analysis. In G012, previous estimates of H_2 column density map (Dell'Ova et al., 2024) lack the full coverage captured by the N_2H^+ map at 3 mm. Here, the H_2 column density map from Dell'Ova et al. (2024) is the best tool with which to estimate the relative abundance in G012; this maps was constructed based on the technique of Point Process MAPping (PPMAP), using continuum observations in band 6 and 3 (ALMA-IMF LP), APEX/LABOCA (870 μm), SABOCA (350 μm), Herschel/SPIRE (250 μm, 350 μm, and 500 μm), PACS (70 μm, 160 μm), SOFIA observations (53 μm - 214 μm), and Spitzer (MIPS and GLIMPSE). To take full advantage of the N_2H^+ data, we use the N_2H^+ column density to estimate the total masses (M_{tot}) in the protocluster as a whole, and in areas where the H_2 map lacks complete coverage. Our method is described below, and is based on the Sandoval-Garrido et al. (2024) procedure.

First, we calculate the relative abundance or average ratio between both N_2H^+ and H_2 column density maps (see Eq. 3.4.1) where we have coverage in both. To estimate this ratio, we reproject the N_2H^+ image to match the pixel scale of the H_2 data, which is slightly larger (with a pixel scale of 0.83). The reprojection can introduce artifacts at the data boundaries because in particular the N_2H^+ regions with sufficient signal to noise (see above) are highly irregular. This irregularity in the spatial distribution can induce artificially low values at the boundaries of the emission, if not addressed properly. To mitigate these effects, we conducted a test following the methodology described in Sandoval-Garrido et al. (2024). Specifically, we identify the portion of the N_2H^+ column density image impacted by the reprojection following the steps below:

1. Creating a mask map: We generated a binary map from the N_2H^+ column density data, assigning a value of 1 to valid data pixels and 0 to the pixels below our signal to noise cut (see above).

2. Reprojecting the mask map: This binary map was reprojected to the Dell'Ova et al. (2024) H_2 pixel scale. Pixels affected by reprojection artifacts were identified as having intermediate values between 0 and 1. We observed that the boundaries of the reprojected image were affected, with typical impacts

extending 1-3 pixels around the map edges, as expected.

3. Defining a final mask: Based on the above results, we defined a mask to exclude pixels impacted by reprojection artifacts. That is, all pixels with values < 1 in the binary mask are excluded from the regridded N_2H^+ column density map.

This process produces an N_2H^+ column density map reprojected onto the H_2 map coordinate system that is free from reprojection artifacts.

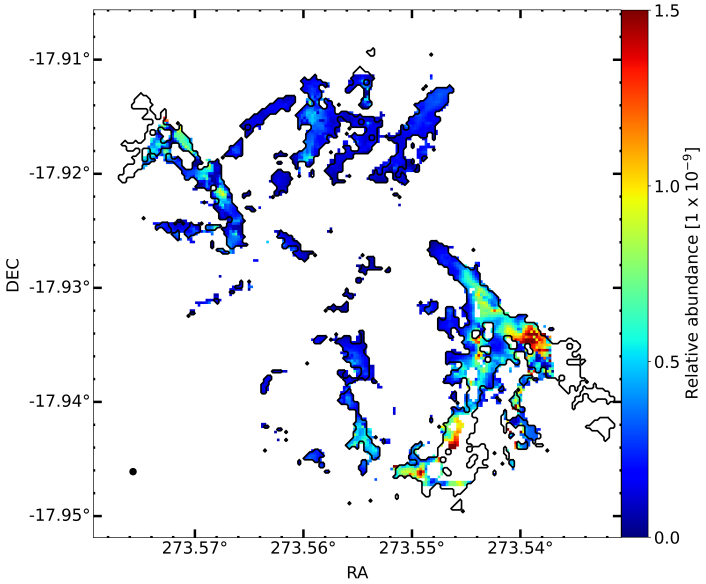

Figure 3.4.1: Relative abundance map in G012. The black contour highlights the mask of $\frac{\tau}{e(\tau)} > 2$ applied to the column density; most of the pixels removed by this mask do not affect the main filaments significantly. The areas lacking data (top of R1 and bottom of R2) are due to the H_2 column density map lack of coverage in the filaments. Inside the contour we find a representative relative abundance value of 9.3×10^{-11} (see text). The black circle in the bottom-left corner represents the beam size of the H_2 map.

Subsequently we calculate a relative abundance map by taking the pixel-to-pixel ratio of the two maps:

$$X(N_2H^+) = \frac{N(N_2H^+)}{N(H_2)} \tag{3.4.1}$$

Here, $N(N_2H^+)$ is the N_2H^+ column density map described above, and $N(H_2)$ is the H_2 column density map from Dell'Ova et al. (2024) (see above). For the $N(H_2)$ map, we consider a $S/N > 3$ based on the ratio between the column density and the associated errors. In Figure 3.4.1, we show the resulting relative abundance

map.

To analyze the distribution of the relative abundance values, we construct a histogram using the Freedman-Diaconis method to determine the optimal bin width and number of bins for the distribution, following Sandoval-Garrido et al. (2024). This method incorporates key statistical metrics, including the first quartile (Q1), third quartile (Q3), interquartile range (IQR = Q3 - Q1), and the overall data range. Using this approach, we determined an optimal bin width of 3.77×10^{-11}, resulting in a total of 40 bins for the distribution. To estimate a representative value for the relative abundance, we selected the mode, or the most prominent bin. We note that previous studies have shown that the mode, in relative abundance maps, remains consistent even when different numbers of bins are used (see Sandoval-Garrido et al., 2024).

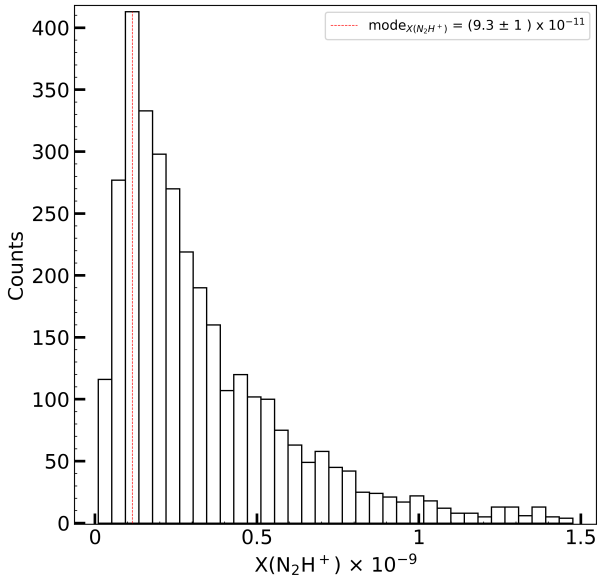

Figure 3.4.2: Relative abundance histogram of the values inside the black contour in Figure 3.4.1. The red-dashed line represents the mode of the distribution. In the upper-right corner, the values of the mode and standard deviation are shown, which we consider as the representative value and error of the sample.

Considering the full sample, the mode in the most prominent bin is of 8.4×10^{-11}. Up to this point, we had adopted relatively conservative error limits for the τ parameter (i.e., $\frac{\tau}{e(\tau)} > 1$, see Sec. A1) to estimate the N_2H^+ column density. To test the effect of more stringent limits and their effect in the relative abundance estimates, we applied progressively stricter masks to the N_2H^+ column density, specifically:

1. $\frac{\tau}{e(\tau)} > 1.5$ ($\sim 3\%$ pixels removed)
2. $\frac{\tau}{e(\tau)} > 2$ ($\sim 7\%$ pixels removed)
3. $\frac{\tau}{e(\tau)} > 3$ ($\sim 15\%$ pixels removed)

For each, we recalculated the relative abundance using the same methodology described above. We found that the mode of the distribution consistently resulted in values in the range between 8.4×10^{-11} to 10.7×10^{-11}, despite slight variations in the number and width of the bins. To avoid the potential effect of high τ errors in the relative abundance estimation, we adopted the mode derived using the $\frac{\tau}{e(\tau)} > 2$ mask, which preserves most of the information in the relative abundance map (only excludes $\sim 7\%$ of pixels) and minimally impacts the filamentary structures in the region. Therefore, the final relative abundance value adopted for the overall region is of $X(N_2H^+) = (9.3 \pm 1) \times 10^{-11}$ (see Figure 3.4.2). We use this value to estimate the masses associated with the line-mass profiles in Sec. 4.2 and, consequently, to analyze the kinematic profile in the R1 filament in Sec. 5.

3.5 N_2H^+ and DCN core velocity estimates

Cores represent the immediate sites of star formation and allows us to investigate the kinematic relationship between the dense gas filaments and the forming protostars. Here we estimate velocities of cores detected in catalogs described in Sec. 2 by using N_2H^+ and DCN spectral lines. First, we verified how many of the previously detected cores in DCN are also detected in N_2H^+. Out of the 38 cores in Cunningham et al. (2023), 36 have N_2H^+ detections with $S/N > 12$.

We also use cores detected by Armante et al. (2024), which include a total of 63 detections, in addition to those previously detected in Cunningham et al. (2023). These 63 cores do not present velocity estimates. To derive velocity measurements we fit both DCN and N_2H^+ emission, using only S/N data > 5 and > 12 respectively, with one Gaussian velocity component (see Appendix A1 for line fitting and S/N definition). We use the size of the major and minor axes of each core (see Table A4.1 and Table A4.3) to define a region where we estimate the average spectrum, the associated velocity center, and the mean of all other `PySpecKit` parameters and errors from the line fitting. One core was excluded from the analysis described below due to poor spectral quality.

From the Armante et al. (2024) catalog, we find a total of 26 cores detected in both tracers (hereafter the DCN ∪ N_2H^+ sample), 22 cores detected only in N_2H^+ (hereafter the N_2H^+ sample), 3 cores detected only in DCN data (hereafter the DCN "new" sample), and 11 cores not detected in any of these two tracers (hereafter the 1.3 mm sample).

For DCN and N_2H^+, we follow the method outlined in Cunningham et al. (2023), and define V_{DCN} and $V_{N_2H^+}$ as the velocity centroid of the core resulting from the DCN and N_2H^+ fits. As DCN has previously proven effective in estimating core velocities, and traces denser and more compact emission than N_2H^+, we prefer the velocities measured with DCN for cores in the DCN ∪ N_2H^+ sample. To validate the use of N_2H^+ velocities for cores lacking DCN velocity estimates (the N_2H^+ sample), we calculated the velocity difference between DCN and N_2H^+, $V_{DCN} - V_{N_2H^+}$ (a similar procedure was perform for the G353.41 protocluster in Álvarez-Gutiérrez et al., 2024), for a total of 62 cores detected in both tracers (36 cores from the previous DCN catalog, and 26 cores from the DCN ∪ N_2H^+ sample).

On average, we found that the N_2H^+ velocities in the core samples are redshifted by approximately 0.1 km s^{-1} compared to the DCN core velocities, in a similar manner as described by Álvarez-Gutiérrez et al. (2024). This difference represents a small fraction of the N_2H^+ (0.23 km s^{-1}) and DCN (0.34 km s^{-1}) velocity resolution. With the approach described above we increase the core velocities sample from 51 cores (26 cores from the DCN ∪ N_2H^+ sample, 22 cores from the N_2H^+ sample, and 3 cores from the DCN "new" sample).

Chapter 4

R1 & R2 analysis

The R1 & R2 filaments are the predominant N_2H^+ integrated intensity structures (see Sec. 3). These regions present highly different velocity structures and cores masses, suggesting the presence of multiple star forming environments taking place in the same protocluster. In this section we focus in the characterization of these two filaments, aiming to set constraints on their star forming stage.

Table 4.0.1: Global parameters of the R1 & R2 filaments

Region	Length pc	Width pc	$<V>^a$ km/s	$<\sigma>^a$ km/s	$<\tau>^a$	M_f^b $10^3\,M_\odot$	M_f/M_{tot}^c
R1	0.56	0.22	34.4 ± 0.05	0.81 ± 0.05	1.96 ± 1.4	1.78	0.12
R2	0.56	0.22	36.8 ± 0.07	0.75 ± 0.06	2.49 ± 1.8	2.53	0.17

(a) Mean of the FVC and SVC fitted parameters. (b) Total H_2 filament mass determined by $N(N_2H^+)$. (c) Fraction of the filament mass respect to the total protocluster mass, where for the G012 protocluster $M_{tot} = 14.8 \times 10^3\,M_\odot$ (see Sec. 3.3).

4.1 R1 & R2 average filament velocity gradients

Above, we highlight the kinematic differences in the PV diagrams along the extent of the R1 & R2 filaments. Specifically, the R1 filament is associated with a potential signature of filament rotation (e.g., Álvarez-Gutiérrez et al., 2021), while R2 presents a relatively compact velocity distribution (see Fig. 4.1.1, upper-right panel). Here we begin by analyzing the velocity gradients perpendicular to both filaments through average-velocity gradients estimations. We use an adaptation of the method described Álvarez-Gutiérrez et al. (2021) and divide the procedure into the following steps:

1. We determine the total integrated intensity in each region (i.e., the moment 0 of the FVC and SVC, see above) and calculate peak integrated intensity values along the long axis of both filaments in order to determinate a representative filament ridgeline. In Appendix A2 we show this procedure for the R1 filament.

2. For each slice along the Y axis we straighten both filaments by centering the peak integrated intensity from the ridgeline to a fixed arbitrary position. This is applied for the data in the integrated intensity (see Fig. A2.1), velocity centroids, and velocity dispersion. After this step, each point has a projected radius to the center of the filament.

3. We generate “average" PV diagrams as follows. For each point, at each projected radius from the ridgeline, we plot the radial velocities. Here the color of each point indicates their integrated intensity. These velocity vs. projected radius diagrams therefore capture PV structures integrated over the length of the filament. If a given filament has a prominent velocity gradient approximately perpendicular to the ridgeline, these diagrams will reveal these structures. This is the case for R1 (and see below), while for R2 no such equivalently prominent structure is observed.

4. We apply a linear fit to the velocity gradient in the R1 filament, taking as a weights for each point their integrated intensity.

In Fig. 4.1.2 we show the R1 (l.h.s.) and R2 (r.h.s.) ridgeline-averaged PV diagram described above. The global R1 velocity gradient has a magnitude of $\mathrm{VG} = 10.4\,\mathrm{km\,s^{-1}\,pc^{-1}}$ (with an associated statistical fitting error of $\pm$ $0.29\,\mathrm{km\,s^{-1}\,pc^{-1}}$).

In R2, as mentioned above and in sharp contrast to R1, we do not observe an equivalent global average velocity gradient. On the contrary, R2 is dominated by a compact velocity structure, clumping at velocities around $\sim 1\,\mathrm{km\,s^{-1}}$ in the center of the diagram. Spatially, this feature traces the central and densest part of the filament. We also observe $\sim$ 3 different additional features that are spatially related with different regions of R2 outside of the ridgeline. These are subdominant and characterized by lower integrated intensity values. For example, we can appreciate a more spread out structure extending up and to left in the diagram and ending near - 0.05 pc, $0.75\,\mathrm{km\,s^{-1}}$. This structure is associated with

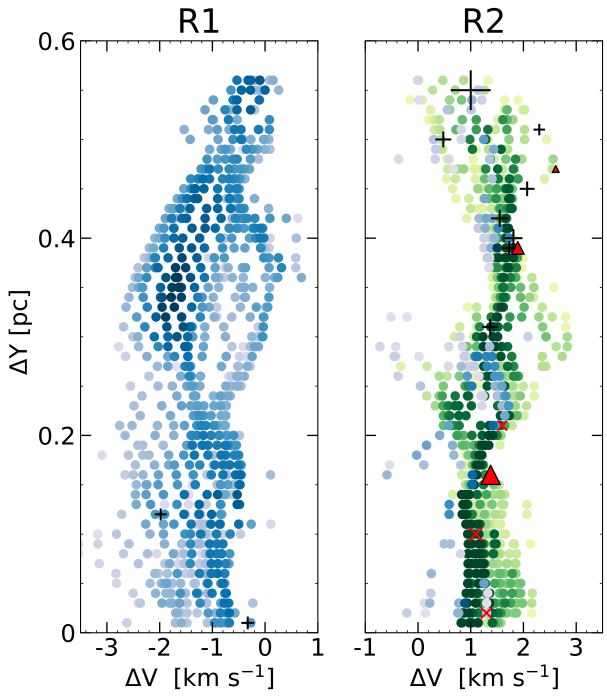

Figure 4.1.1: PV diagrams of R1 (l.h.s.) & R2 (r.h.s.) with the cores (with the same color scheme and symbols as in Fig. 3.2.1). These diagrams highlight the different structures in each region. R1 presents a wrapping "double-helix" signature that is most obvious toward the top of the diagram and which is dominated by the FVC velocities (blue color scale, as in Fig. 3.2.1). R2 exhibits comparatively compact velocity variations and smooth positional undulations along the filament, and contains a high number of massive cores.

the $\sim$ eastern edge of the R2 filament, and has associated elongated SiO emission likely tracing protostelar outflows and shocks (Towner et al., 2024).

4.2 R1 & R2 line-mass profiles and associated 3D model quantities

Characterization of the mass distribution, and hence of the gravitational potential, is an absolute requirement for interpreting the kinematics in these systems since the gravitational field of the gas serves as governor of the dynamics of a system (e.g., Stutz and Gould, 2016). Here we use the above mass estimates derived to obtain the average line-mass profiles in the R1 & R2 filaments.

Since Dell'Ova et al. (2024) mass map lacks full coverage the of the R1 filament, we use mass estimates from Sec. 3.4, which are derived from the N_2H^+ data and

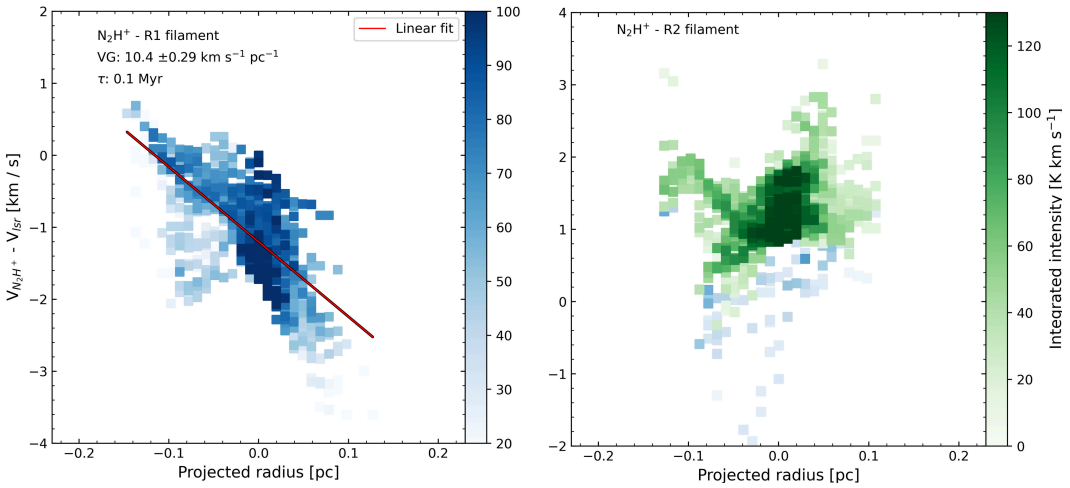

Figure 4.1.2: Average velocity gradients perpendicular to R1 (l.h.s.) & R2 (r.h.s.) filaments. In both diagrams, the ΔV and Δr axes have the same range, allowing for direct comparison of slopes between panels. In R1 the red line represents the linear fit weighted by the integrated intensity points of the velocity gradient (VG). The associated VG timescale (τ) estimation is displayed in the upper left corner. On the other hand, R2 lacks a clear velocity gradient structure as in R1 and is instead comparatively compact. In addition, we identify three different structures that spatially correspond to different regions in this R2 diagram. The most compact and central structure is related to the densest region of the filament. The most elongated feature is spatially related to the eastern edge of the R2 filament, characterized by the presence of elongated SiO emission. In the diagram, the lower intensity and scattered points represent regions surrounding the filament.

calibrated to the measurements by Dell'Ova et al. (2024). In order to validate our mass map selection, we calculate the line-mass profile in a portion of R2 filament that has coverage in both N_2H^+ and Dell'Ova et al. (2024) column density maps (see Appendix A3). We find minor variations, less that 28%, between the two methods. Therefore, we adopt the N_2H^+ mass map to estimate the line-mass profiles below.

We follow the formalism outlined in Stutz and Gould (2016) to estimate these line-mass profiles (see also González Lobos and Stutz, 2019; Stutz, 2018; Álvarez-Gutiérrez et al., 2021; Reyes-Reyes et al., 2024). Briefly, we first align the filament mass maps with respect to their ridgelines (see Appendix A2). We use a box size of 0.56 pc × 0.22 pc (box length × box width) to capture the densest parts of both filaments, shown in Fig. 1.0.1, right panel. We then construct N_2H^+ cumulative mass distributions for both filaments. As expected for elongated and

Table 4.2.1: Line-mass profiles, volume density, gravitational potential, and acceleration distributions

Region	ζ^a $M_\odot pc^{-1}$	β^b $M_\odot pc^{-3}$	ψ^c $km^2 s^{-2}$	ξ^d $km^2 s^{-2} pc^{-1}$	γ^e	Projected Length^f pc	Total Gas Mass^g $M_\odot$
G012.80-R1	5660	211.3	123.1	37.4	0.30	0.56	1780
G012.80-R2	6943	181.3	269.3	51.3	0.20	0.56	2532
L1482-S^h	205	9.60	1.27	0.81	0.64	0.90	380
ONC^h	866	25.9	27.6	6.40	0.23	0.50	1300
Orion ISF^h	385	16.5	6.30	2.40	0.38	7.30	6200
G351.77^h	1660	78.7	13.5	8.38	0.62	8.60	10200

Normalization constants for: (a) the M/L profile in Eq. 4.2.1, (b) the volume density in Eq. 4.2.3, (c) the gas gravitational potential in Eq. 4.2.4, and (d) the gravitational acceleration in Eq. 4.2.5. (e) Power-law index in the M/L profile. (f) Filament length for the M/L estimates (see Sec. 4.2). (g) Total gas mass in the filaments (see Sec. 4.3). (h) Regions described in Sec. 4.2 and shown in Fig. 4.2.1.

dense structures, we find that the cumulative mass distribution profiles in both R1 and R2 are almost linear (see Fig. A3.2), meaning that the mass distribution along the filament is approximately uniform. This permits averaging a line-mass profile as a function of projected radius from the ridgeline, over the filament as a whole.

Following the formalism in Stutz and Gould (2016), and the above references, we find that the line-mass profiles are well-described by power laws of the form:

$$\lambda_{app}(\omega) = \zeta \left(\frac{\omega}{pc} \right)^{\gamma}, \tag{4.2.1}$$

where ω is the projected radius in the POS (or impact paramenter from the ridgeline), γ corresponds to the index in the enclosed mass over length (M/L) vs. projected radius diagram (see Fig. 4.2.1), and ζ is the M/L normalization constant. For R1 and R2 we obtain:

$$\begin{aligned} \zeta_{R1} &= 5660 \frac{M_\odot}{\text{pc}}, \quad \gamma_{R1} = \frac{3}{10}, \quad \lambda_{R1}(\omega) = 5660(\omega/\text{pc})^{0.30}; \\ \zeta_{R2} &= 6943 \frac{M_\odot}{\text{pc}}, \quad \gamma_{R2} = \frac{1}{5}, \quad \lambda_{R2}(\omega) = 6943(\omega/\text{pc})^{0.20}. \end{aligned} \tag{4.2.2}$$

In Fig. 4.2.1, we display the M/L profiles of the R1 & R2 filaments (red and blue lines), along with with other star-forming regions (black dashed lines) described below and in Table 4.2.1.

We follow Stutz and Gould (2016); Stutz (2018); Álvarez-Gutiérrez et al. (2021) to estimate the density, gravitational potential, and acceleration assuming cylindrical 3D geometry, which will also be useful for comparison with other protoclusters. All quantities are estimated in the POS since we do not have access to inclination information (and see below). We refer to these as “apparent" profiles following Álvarez-Gutiérrez et al. (2021). We estimate the apparent volume density as:

$$\rho_{app}(r) = \beta \left(\frac{r}{\mathrm{pc}} \right)^{\gamma-1}, \tag{4.2.3}$$

where for the R1 & R2 filaments, we obtain $\beta_{R1} = 211.3\,\mathrm{M_\odot\,pc^{-3}}$ and $\beta_{R2} = 181.3\,\mathrm{M_\odot\,pc^{-3}}$. We estimate the gravitational potential as:

$$\phi_{app}(r) = \psi \left(\frac{r}{\mathrm{pc}} \right)^{\gamma}, \tag{4.2.4}$$

where, considering the R1 & R2 parameters described above, we estimate $\psi_{R1} = 123.1\,\mathrm{km^2\,s^{-2}}$ and $\psi_{R2} = 269.3\,\mathrm{km^2\,s^{-2}}$. Finally, we estimate the gravitational acceleration as follows:

$$g_{app}(r) = -\xi \left(\frac{r}{\mathrm{pc}} \right)^{\gamma-1}. \tag{4.2.5}$$

For R1 & R2 we obtain $\xi_{R1} = 37.4\,\mathrm{km^2\,s^{-2}\,pc^{-1}}$ and $\xi_{R2} = 51.3\,\mathrm{km^2\,s^{-2}\,pc^{-1}}$, respectively.

For simplicity, we assume the inclination angle (θ) of the filaments with respect to the POS to be zero in all previous equations. In Table 4.2.1 we include previous M/L profiles estimations for the parent filament of G351.77 protocluster, the Orion Nebula Cluster (ONC), the Orion ISF, and the California L1482-S cloud (Stutz and Gould, 2016; Stutz, 2018; Álvarez-Gutiérrez et al., 2021; Reyes-Reyes et al., 2024). Relative to other star-forming regions (Table 4.2.1 and Fig. 4.2.1), the filaments in G012 exhibit significantly higher line-mass profiles, up to three times more massive than extended regions such as the G351.77 protocluster.

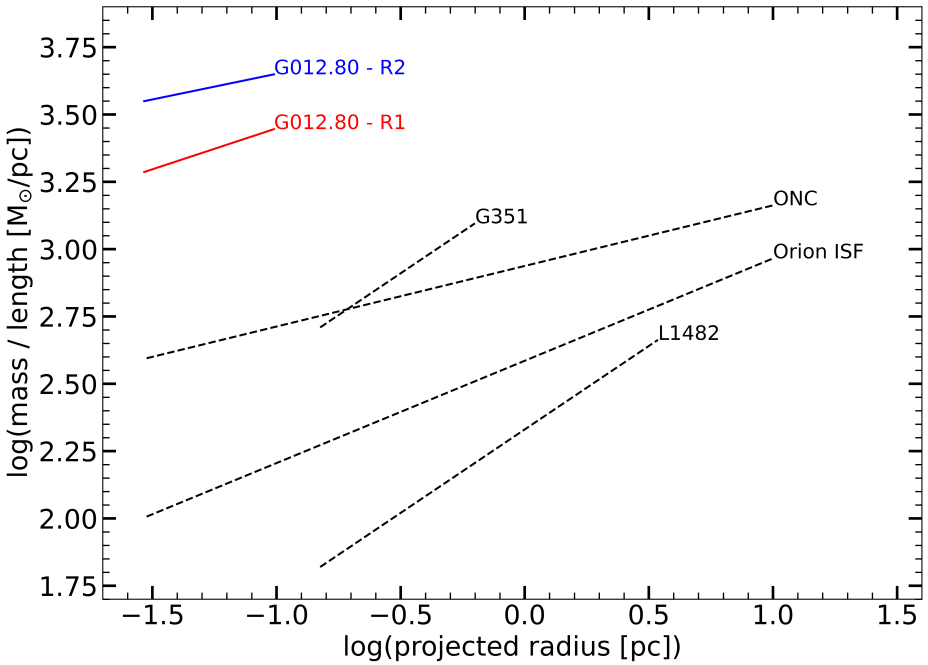

Figure 4.2.1: Line-mass profile of the R1 & R2 filaments (red and blue lines). We include profiles of the Orion ISF, the ONC, the California L1482 regions, and the G351.77 protocluster (black lines). The main filaments of G012 reveal higher line-mass distributions than those found in other star-forming regions compared to here.

4.3 Star formation rate and efficiency in the R1 & R2 filaments

The star formation rate (SFR) and efficiency (SFE) are critical parameters to understand the current star formation activity, offering insight into the efficiency in which gas is converted into stars. The SFR and SFE provide key metrics to evaluate in combination with the kinematics (see below). This also permits a comparison to other systems that have been characterized in a similar fashion. For the SFR and SFE estimates, we use the formalism outlined in Megeath et al. (2022) and consider the core masses provided in Motte et al. (2024, accepted).

To estimate the SFR (Eq. 4.3.1), we assume lifetimes based on observational studies of stellar cores. The lifetimes of prestellar cores, typically associated with the slow gravitational contraction of low-density material, have been estimated to be around 1 Myr in nearby molecular clouds (Jessop and Ward-Thompson, 2000; Könyves et al., 2015). For protostellar cores, studies suggest lifetimes between

200 kyr and 500 kyr, depending on the mass regime (Duarte-Cabral et al., 2013; Megeath et al., 2022, Valeille-Manet et al. submitted).

In the R1 & R2 filaments, Armante et al. (2024) and Motte et al. (2024, accepted) identified a total of 16 cores. Fourteen of these are located in R2, and only 2 are in R1. These cores are classified as either being prestellar or protostellar (Armante et al., 2024, Motte et al. accepted), with masses ranging from 0.3 to 5 $M_\odot$. For our analysis, we adopt a prestellar timescale of 1.2 Myr, the expected value for prestellar cores in the mass range of 0.003 - 10 $M_\odot$(Könyves et al., 2015). We also use protostellar lifetime of 0.5 Myr, assuming a low-mass protostellar regime around 0.5 $M_\odot$ (Megeath et al., 2022).

Both cores in R1 are clasified as prestellar, while the R2 filament exhibits five cores in this phase. In addition, the R2 filament contains 9 protostellar cores. Considering the pre- and protostellar lifetimes described above, we estimate the SFR as follows:

$$\mathrm{SFR}(\mathrm{M_\odot Myr^{-1}}) = \frac{\mathrm{M_{cores}}}{\mathrm{t_{cores}}}. \tag{4.3.1}$$

Here, M_{cores} is the mass of the prestellar/protostellar core population and t_c is the approximate lifetime of the prestellar/protostellar cores in Myr. For the R1 and R2 filaments, we obtain:

$$\begin{aligned}
&\mathrm{SFR_{R1\text{ - }prestellar}} = 4.24\ \mathrm{M_\odot\ Myr^{-1}},\\
&\mathrm{SFR_{R2\text{ - }prestellar}} = 12.1\ \mathrm{M_\odot\ Myr^{-1}},\\
&\mathrm{SFR_{R2\text{ - }protostellar}} = 43.2\ \mathrm{M_\odot\ Myr^{-1}},\\
&\mathrm{SFR_{R2\text{ - }total}} = \mathrm{SFR_{prestellar}} + \mathrm{SFR_{protostellar}} \rightarrow 55.3\ \mathrm{M_\odot\ Myr^{-1}}.
\end{aligned} \tag{4.3.2}$$

For intermediate to high-mass regime (with a lifetime of 0.3 Myr), the SFR could potentially increase to 84 $M_\odot$ Myr^{-1}.

In addition, we estimate the SFE as:

$$\mathrm{SFE} = \frac{\mathrm{M_{cores}}}{\mathrm{M_{cloud}} + \mathrm{M_{cores}}}. \tag{4.3.3}$$

In this case M_c represents the same core mass used for the SFR estimate, and

M_{cloud} corresponds to the R2 filament mass (see Table 4.0.1). In the R1 and R2 filaments, we obtain:

$$\begin{aligned}
&\mathrm{SFE}_{\text{R1 - prestellar}} = 0.002,\\
&\mathrm{SFE}_{\text{R2 - prestellar}} = 0.003,\\
&\mathrm{SFE}_{\text{R2 - protostellar}} = 0.005,\\
&\mathrm{SFE}_{\text{R2 - total}} = \mathrm{SFE}_{\text{prestellar}} + \mathrm{SFE}_{\text{protostellar}} \rightarrow 0.008.
\end{aligned} \tag{4.3.4}$$

The absence of protostellar cores and the limited presence of prestellar cores in the R1 filament suggest notable differences in the evolutionary status of the cores in both filaments. These differences imply that R1, compared to R2, might exist in an earlier evolutionary stage that has not (yet) achieve the central filament concentration and star formation that R2 is undergoing today. The detection of a pronounced velocity gradient in R1, combined with the almost complete absence of any such equivalent structure in R2, tends to corroborate the above evolutionary scenario (and see below).

Chapter 5

A filament rotation model applied to R1

In the N_2H^+ PV diagram, the R1 filament shows a helical pattern, a feature also observed in the California L1482-S cloud and attributed to filamentary rotation (Álvarez-Gutiérrez et al., 2021). In Fig. 4.1.1 (left panel), we highlight this feature at the top of R1 which is also associated to a clear average-velocity gradient of $\sim$10.4 km s^{-1} pc^{-1} in Fig. 4.1.2 (left panel). To determine if rotation or gravity is the dominant factor in the R1 filament, we compare the estimated gradient to the filament mass distribution.

We apply the formalism from Álvarez-Gutiérrez et al. (2021) to estimate the centripetal force associated to the rotation of the R1 filament, and also to derive the gravitational force. We then calculate the ratio between both forces as follows:

$$\frac{F_c}{F_g} = \frac{v^2 pc^{-1}}{\xi cos^3(\theta)} \left(\frac{r}{pc}\right)^{-\gamma}; \quad v = 10.4 \ \frac{\text{km}}{\text{s pc}}, \ \xi = 37.4 \ \frac{\text{km}^2}{\text{s}^2 \ \text{pc}}. \tag{5.0.1}$$

Here, F_c and F_g represent the centripetal and gravitational forces, v is the average-velocity gradient along the R1 filament, ξ is the constant associated with the gravitational acceleration distribution (see Table 4.2.1), and θ represents the inclination angle of the filament relative to the plane-of-sky (POS).

In Fig. 5.0.1, we present the resulting profile for the ratio of forces in the R1

filament (red line), assuming $\cos(\theta) = 1$. The R1 profile indicates that the filament is predominantly influenced by gravity rather than rotation, similar to the internal rotation pattern observed in the California L1482-S cloud (dashed-grey line). The high line-mass profile seen in the R1 filament, combined with the gravitational dominance in this profile, suggest that the filament is primarily supported by gravity, even in the presence of rotation.

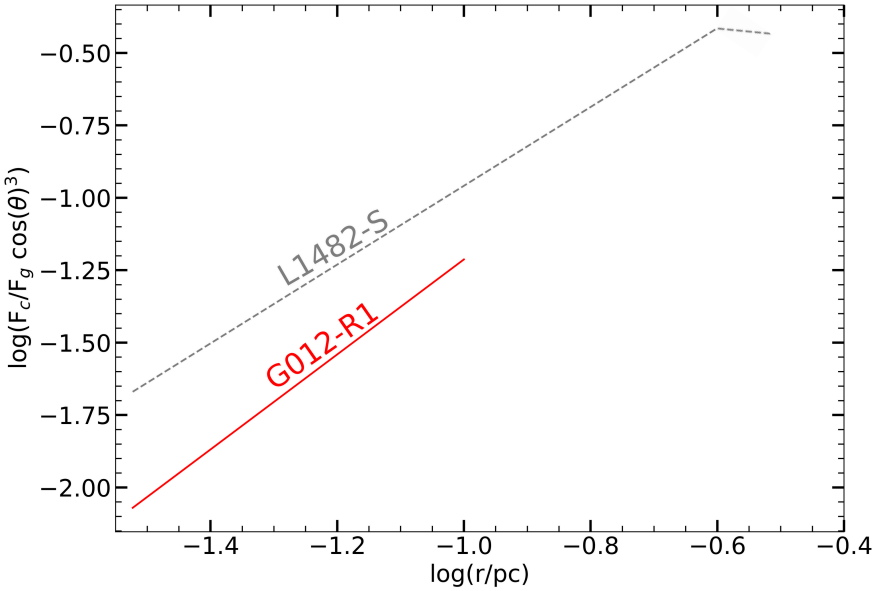

Figure 5.0.1: Ratio between the centripetal (F_c) and gravitational (F_g) forces in the R1 filament (red line), where θ represents the inclination angle of the filament relative to the plane-of-sky (POS). We assume $\cos(\theta) = 1$, corresponding to a filament aligned with the POS. For N_2H^+, the gravitational force dominates over rotational force, with a distribution similar to the internal rotation observed in the California L1482-S filament (Álvarez-Gutiérrez et al., 2021).

In contrast with California L1482-S, we not observe rotation in the $C^{18}O$ gas in the R1 filament. The observation of rotational motion in star-forming regions traced by different molecular species can provide insights into their evolutionary stages. If the rotation is observed in $C^{18}O$ emission (Álvarez-Gutiérrez et al., 2021), it could indicates an earlier evolutionary phase compared to rotation traced by N_2H^+ (R1 filament). These two molecules trace distinct physical conditions within molecular clouds, revealing differences in density, temperature, and chemical composition, which evolve over time in a star-forming region (e.g., Tafalla et al., 2004; Tanaka et al., 2013).

$C^{18}O$ is a stable isotopologue of CO and tends to remain in the gas phase in

environments that are relatively warm and have lower densities. Consequently, $C^{18}O$ serves as an effective tracer for gas that has not yet reached the conditions necessary for significant CO depletion, which is common in the early stages of cloud collapse (e.g., Tafalla et al., 2004; Friesen et al., 2010; Punanova et al., 2016). As the cloud evolves and contracts under gravity, it cools and reaches densities that favor the depletion of CO onto dust grains, creating conditions suitable for the formation and stability of N_2H^+ (Caselli et al., 2002). This progression from gas traced by $C^{18}O$ to N_2H^+ highlights the changes in physical conditions as a molecular cloud transitions from a quiescent state to a denser, active star-forming region.

Consequently, although both the California L1482-S region and R1 share similar kinematic features and low core formation rates, the R1 filament appears to be in a slightly more advanced evolutionary phase.

Chapter 6

Discussion

Despite the morphological similarities between the two main G012 filaments, our analyses revealed differences in their gas kinematics, mass distributions, and cores population. In the following discussion, we explore the different star-forming scenarios that may be associated with the R1 and R2 filaments, emphasizing their potentially different evolutionary paths.

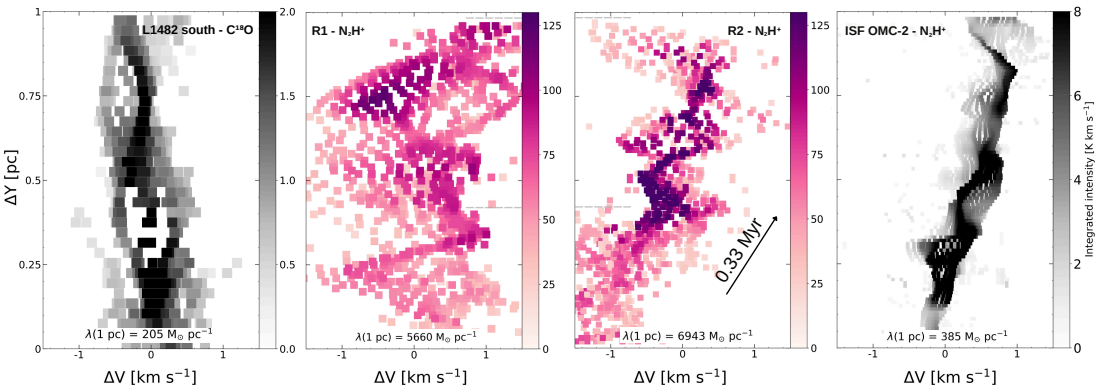

Figure 6.0.1: Comparative PV diagrams of California L1482-south (left panel), OMC-2 (right panel), R1 & R2 filaments (center panels). Similar to California, R1 presents a "double helix" feature, low presence of cores, and low temperatures (< 25 K, see Dell'Ova et al., 2024). Despite this, line-mass profile of both regions (estimated within the range of the gray lines) shows that R1 is more massive than California L1482-south. On the other hand, R2 shows PV diagram features compare to ISF OMC-2 region. Specifically, R2 presents smooth undulations in velocities characterized with uniform velocities. R2 is also characterized by a high presence of cores, indicating that the gas velocities should be mostly influenced by the accretion of these sources.

6.1 Core accretion signatures in the R2 filament

Recently, Dell'Ova et al. (2024) estimated a dust temperature map in the G012 protocluster, finding temperatures of around 35 K at the beginning of the R2 filament. In addition, they also found a spatial shift at the top of the filament between the peak column densities of $H_2$and N_2H^+ (see Fig.,10 in Dell'Ova et al., 2024). To explain this shift, they propose a scenario in which a detected hot core (Armante et al., 2024) is heating the region and destroying the N_2H^+ emission at the top of the filament. In this case, the accretion scenario could be consistent with the small spreads in velocity that we observed in the R2 filament, as well as the absence of N_2H^+ in the hot core location.

Previous studies link core accretion in filaments with "V-shapes" structures in PV diagrams (e.g., Álvarez-Gutiérrez et al., 2024; Sandoval-Garrido et al., 2024). The N_2H^+ PV diagram in R2 lacks these kind of features, mainly because N_2H^+ is absent at the top of R2. However, we observed that the DCN emission reveals a clear V-shape in the same region where the detected hot core is located, along with an SiO elongated structure perpendicular to the top of R2 (see Fig. 3 in Armante et al., 2024). This suggests that the V-shaped feature traced by DCN at the hot core location is related to a strong outflow and, consequently, to potential accretion processes at the top of R2.

In addition, as shown in Fig. 4.1.2 (right panel), we observe that the velocities associated with the central and densest region of the filament are clumping at the center of the average-velocity diagram. This clumping structure at $\sim 1\,\mathrm{km\,s^{-1}}$ could indicates the presence of dense structures within the R2 filament (accumulations of gas), as is observed in the integrated intensity map, suggesting ongoing accretion processes in the protocluster (e.g., Hacar et al., 2013; Kainulainen et al., 2016; Ladjelate et al., 2020). Such structures in PV space can be indicative of the formation of dense cores, which are crucial for star formation, as they represent regions where the gravitational forces outweigh the thermal pressures of the surrounding medium (e.g., André et al., 2010; Palau et al., 2013). Therefore, this clumping structure highlights the kinematic complexity within the filament that is apparent dominated by their cores.

In our comparative assessment of the R2 filament and other star-forming regions, we analyzed the star formation rate and efficiency for protostellar

cores in the ISF OMC-2 region (Megeath et al., 2012, 2016; Furlan et al., 2016; Kainulainen et al., 2017; Stutz, 2018; González Lobos and Stutz, 2019), obtaining a SFR = 95 $M_\odot$ Myr^{-1} and a SFE = 0.008. In addition, previous studies estimated a line-mass profile of $\lambda(\omega) = 385(\omega/\mathrm{pc})^{0.38}$ in this region (Stutz, 2018). Interestingly, while the R2 filament has a more pronounced line-mass profile, it forms prestellar and protostellar cores at a similar but lower SFR than that observed in the ISF OMC-2 (see Sec. 4.3), with both regions exhibiting comparable efficiencies. Considering the line-mass profile in the R2 filament, along with the distinct kinematic features presented in this study, the R2 filament could be in an evolved state, possibly earlier but still comparable to regions like the ISF OMC-2.

6.2 Timescales of the prestellar and protostellar cores

The formation of stellar objects occurs over diverse timescales, reflecting the intricate processes governing their evolution (Bergin and Tafalla, 2007; Evans et al., 2009; Dunham and Vorobyov, 2012; Dunham et al., 2014; Motte et al., 2018). Prestellar and protostellar cores represent distinct phases in star formation, each characterized by specific physical conditions and evolutionary mechanisms. Understanding these timescales is essential to set further constraints on the processes shaping star-forming environments and their evolution.

Prestellar cores are believed to be the initial gravitationally bound structures that precede star formation. The timescale associated to the evolution of these cores can vary significantly depending on environmental factors and initial conditions (Motte et al., 2018). Observations suggest that the lifetime of prestellar cores ranges from about 0.5 to 2 Myr (e.g., Jessop and Ward-Thompson, 2000; Merín et al., 2008; Alcalá et al., 2008; Evans et al., 2009; Könyves et al., 2015). The duration of this phase is influenced by the efficiency of the gravitational collapse, which is affected by the core's density and the presence of external pressures from surrounding environment inside molecular clouds (Tafalla et al., 2004; Könyves et al., 2015, Valeille-Manet et al. submitted). For instance, lifetimes for high-mass prestellar cores (PSCs) reported in Valeille-Manet et al. (submitted) tend to be considerably shorter than those observed in low-mass star-forming regions, approximately 0.12–0.24 Myr for cores with masses ranging from 8 to 16 $M_\odot$, and

0.05–0.1 Myr for cores with masses from 30 to 55 $M_\odot$, in which the contraction of massive cores is driven by fast converging flows.

As cores evolve into protostellar phases, the associated accretion timescales decrease. The transition from prestellar to protostellar cores is often marked by significant increases in temperature and density, driven by gravitational contraction and accretion from surrounding material (Bontemps et al., 2010; Dunham et al., 2014). The protostellar phase, particularly in high-mass regimes, also varies with mass (Motte et al., 2018, Valeille-Manet et al. submitted). Studies suggest a decrease in protostellar lifetime with increasing mass, estimated to range from 0.5 Myr in lower masses (e.g., Megeath et al., 2022) to 0.1–0.3 Myr in high-mass cores (e.g., Duarte-Cabral et al., 2013, Valeille-Manet et al. submitted). For instance, Dunham et al. (2014) provides essential insights into the relationship between protostellar core properties and their evolutionary timescales, indicating that the initial mass of a core significantly influences its rate of accretion and subsequent timescale.

The different timescales for prestellar and protostellar cores have significant implications for star formation processes in different environments, particularly in the G012 protocluster. In the R1 filament, which contains only prestellar cores (Armante et al., 2024, Motte et al. accepted), the low SFR of 4.24 $M_\odot$ Myr^{-1} and an SFE of 0.002 indicate a prolonged timescale for star formation, despite the high density of the filament. Conversely, filament R2 exhibits a considerably higher total SFR of 55.3 $M_\odot$ Myr^{-1}, encompassing both prestellar and protostellar cores, with an SFE of 0.008. The presence of multiple protostellar cores in R2 indicates a more dynamic and efficient star formation environment. The higher SFR and SFE suggest that R2 is a more active star formation region than R1, potentially driven by local turbulence or shocks (e.g. by the influence of the hot core detected at the top of the R2 filament, see Armante et al., 2024; Dell'Ova et al., 2024) within the molecular cloud that enhance the accretion processes.

This highlights the complex interplay between core evolution and environmental conditions in determining star formation outcomes. The differences between R1 and R2 illustrate how variations in the core population and their associated timescales can influence the overall protocluster star formation efficiency and the kinematic patterns.

6.3 Different evolutionary stages inside protoclusers

In Fig. 6.0.1, we compare the PV-diagram features and M/L profiles at 1 pc for the R1 & R2 filaments in G012, the G351 filament, the ONC, the Orion ISF, and the California L1482-S region. The key differences observed in the line-mass profiles and PV diagrams emphasize the potentially different evolutionary stages and their impact on filamentary structures, kinematics, and the star formation conditions in the protocluster. By comparing these regions, we gain insights into the progressive changes that occur as filaments evolve from their early (California L1482-S), more chaotic stages to more structured and evolved forms (ISF OMC-2).

Considering all the features revealed in this study, we propose that the R1 filament is still rotating and is younger than R2, in a similar behavior as California L1482-S. In contrast, the R2 filament exhibits kinematics and star formation patterns in congruence with more evolved and efficient stages of star formation, such as that of the ISF. Thus, G012 contains massive filaments at different evolutionary stages.

Recent observations and theoretical studies have demonstrated the presence of filaments in different evolutionary stages within the same protocluster. These findings have provided significant insights into the complex processes of star formation and the role of filamentary structures in guiding the evolution of molecular clouds (Tafalla et al., 2004; André et al., 2010; Schneider et al., 2012; Hacar et al., 2013; Peretto et al., 2014; Zhou et al., 2022). Several investigations highlighted the coexistence of filaments in distinct evolutionary phases, offering a detailed view of the sequential and sometimes parallel pathways through which filaments form stars.

In this context, a common finding is the identification of filaments that display different physical characteristics within a single star-forming region. For instance, Hacar et al. (2013) observed the Taurus cloud, which revealed a 6 pc-long velocity-coherent filament. This filament exhibited regions of near-sonic motions alongside denser and potentially more evolved segments, suggesting different evolutionary phases coexisting within the same cloud. Similarly, Peretto et al. (2014) analyzed the SDC13 system and identified filaments in the early stages of collapse, alongside with more evolved areas that were actively forming stars. The authors concluded

that the different conditions in temperature and density across the cloud were likely responsible for these differences. Schneider et al. (2012), using Herschel data, provided another striking example by studying the Rosette molecular cloud. This work highlighted how filaments in the same cloud can exhibit significantly different densities, temperatures, and levels of fragmentation. Some filaments were at the onset of collapse, while others were already forming dense cores, indicating that different parts of the cloud were evolving at different rates. Similarly, André et al. (2010) observed filamentary networks in the same molecular cloud transitioning from gravitationally unbound filaments to dense star-forming cores.

Several processes can lead to the presence of filaments at different evolutionary phases within a single protocluster. One primary factor is the initial density distribution within the molecular cloud. Denser regions tend to collapse more quickly under their own gravity, leading to the formation of stars, while lower-density filaments remain stable for longer periods. This process is well illustrated in Peretto et al. (2014), where higher density region showed signs of active star formation, while the more diffuse parts of the cloud had not yet collapsed. Additionally, feedback mechanisms from protostellar outflows and winds can affect the evolution of nearby filaments. In environments where stars have already begun to form, their outflows can compress adjacent gas, potentially accelerating the collapse of nearby filaments while preventing others from fragmenting (e.g., Tafalla et al., 2004). André et al. (2010) emphasized how such interactions can result in a wide variety of evolutionary outcomes, even within close proximity.

Another critical factor is the differential accretion of material along filaments. Hacar et al. (2013) proposed that the accretion of gas onto filaments plays a key role in determining their evolution, with some filaments gaining enough mass to trigger collapse while others remain below the critical threshold. This “selective" growth process, driven by local conditions and the amount of available gas, could explain the simultaneous existence of quiescent and collapsing filaments in the same molecular cloud.

Understanding the coexistence of filaments at different evolutionary stages within the same protocluster is crucial for constructing a comprehensive model of star formation. Filaments are recognized as the primary structures through which molecular clouds fragment into star-forming cores (Kirk et al., 2013; Hacar et al., 2013; André et al., 2014; Stutz and Gould, 2016; Stutz, 2018; Hacar et al., 2023;

Louvet et al., 2024). The presence of filaments at different stages of collapse and fragmentation within a single region suggests the star formation is not a “uniform" process, but rather one that is highly dependent on local physical conditions. It also suggests that star formation within a protocluster can occur over extended periods of time. This means that young stellar objects in the same cluster can have significantly different ages, a characteristic that has been previously observed in star-forming regions (Schneider et al., 2012; Peretto et al., 2014). The kinematic interaction between filaments and their surrounding environments also indicates that feedback mechanisms play a crucial role in shaping the star formation history of a molecular cloud.

Chapter 7

Conclusions

G012 is one of the most evolved and massive regions in the ALMA-IMF dataset. Its dense gas emission, traced by the N_2H^+ molecule, reveals a morphology composed of two large filaments and additional irregular but similarly dense structures. The center of G012 presents an absence of N_2H^+, however other tracers indicate the existence of large-scale H II regions, which destroy the dense gas forming a disrupted structure in the protocluster center. In this research we focus on the kinematical analysis of the N_2H^+ emission of the G012 protocluster, including mass distribution analysis, and the characterization of its two main filamentary structures R1 & R2. Our main conclusions are summarized below:

1. We find multiple velocity components in G012. Around 55 % of the spectra are well fitted by two velocity components, while the remainder is well described by a single component. Using a velocity threshold set at $35.6\,\mathrm{km\,s^{-1}}$ we distributed the single velocity component into two velocity component.

2. The integrated intensity map reveals two filamentary structures that we denoted as R1 & R2. Despite their similarity in morphology, we find several differences in their kinematics.

3. R1 is characterize by a velocity gradient in the moment 1 map. We review the PV diagram features which showed a helical structure at the top of the filament associated with filament rotation. We find an average velocity gradient of $\sim 10.4\,\mathrm{km\,s^{-1}\,pc^{-1}}$ (0.1 Myr) in this feature.

4. In the N_2H^+ PV diagrams, R2 is characterize by smooth and compact

velocity undulations. In contrast with R1, R2 lacks a large-scale velocity gradient. However, R2 has a large population of massive cores, relative to R1, and it is associated with a perpendicular SiO outflow at the top of the filament.

5. We estimate line-mass profiles of both filaments that are well described by $\lambda(\omega) = 5660\,(\omega/\mathrm{pc})^{0.30}$ and $\lambda(\omega) = 6943\,(\omega/\mathrm{pc})^{0.20}$ for R1 & R2, respectively. When we compare these distributions with those from other well-studied regions, such as the G351.77 parent filament, the ISF, the ONC, and the L1482 in California, we found that R1 and R2 stand out as being more massive.

6. We compare the centripetal and gravitational forces in the R1 filament finding that the rotation in the filament is subdominant compared with the gas gravitational potential.

7. We calculate SFR and SFE of protostellar cores population in both filaments. R1 lacks protostellar cores, and the few cores present are in prestellar phase. On the other hand, R2 forms protostellar cores at a rate of $\mathrm{SFR} = 55.3\,\mathrm{M}_\odot\,\mathrm{Myr}^{-1}$ with a similar efficiency than the Orion ISF.

8. Using N_2H^+ and DCN spectral lines, we estimate new velocity for 51 previously detected cores. We conclude that the absence of DCN data in some regions should not be a constraint in the study of cores inside molecular clouds. In such cases, the use of N_2H^+ provides a reliable alternative (see also Álvarez-Gutiérrez et al., 2024), allowing the estimation of cores velocities.

9. Considering the different gas and cores kinematics, cores masses, and M/L profiles present in R1 & R2, we propose that R1 is still rotating and younger than the R2 filament, which has further collapsed to a more efficient state of star formation.

The results presented in this study emphasize the role of dense filamentary structures in high-mass star formation, especially when found at different stages of evolution within the same protocluster. Detecting filaments at different evolutionary phases within a single protocluster allows us to characterize multiple stages of star formation, from the earliest accretion processes to later stages of core collapse. By uncovering these kind of filaments, we also gain valuable insights into the diverse mechanisms and chemistry governing gas kinematics including

gas accretion and filament rotation. This ability to observe a “snapshot" of the different stages in one region presents a unique window into the ongoing processes shaping these dense structures.

Bibliography

Alcalá, J. M., Spezzi, L., Chapman, N., Evans, Neal J., I., Huard, T. L., Jørgensen, J. K., Merín, B., Stapelfeldt, K. R., Covino, E., Frasca, A., Gandolfi, D., and Oliveira, I. (2008). The Spitzer c2d Survey of Large, Nearby, Interstellar Clouds. X. The Chamaeleon II Pre-Main-Sequence Population as Observed with IRAC and MIPS. , 676(1):427–463.

Álvarez-Gutiérrez, R. H., Stutz, A. M., Law, C. Y., Reissl, S., Klessen, R. S., Leigh, N. W. C., Liu, H. L., and Reeves, R. A. (2021). Filament Rotation in the California L1482 Cloud. , 908(1):86.

Álvarez-Gutiérrez, R. H., Stutz, A. M., Sandoval-Garrido, N., Louvet, F., Motte, F., Galván-Madrid, R., Cunningham, N., Sanhueza, P., Bonfand, M., Bontemps, S., Gusdorf, A., Ginsburg, A., Csengeri, T., Reyes, S. D., Salinas, J., Baug, T., Bronfman, L., Busquet, G., Díaz-González, D. J., Fernandez-Lopez, M., Guzmán, A., Koley, A., Liu, H. L., Olguin, F. A., Valeille-Manet, M., and Wyrowski, F. (2024). ALMA-IMF XIII: N_2H^+ kinematic analysis on the intermediate protocluster G353.41. *arXiv e-prints*, page arXiv:2404.07363.

André, P., Di Francesco, J., Ward-Thompson, D., Inutsuka, S. I., Pudritz, R. E., and Pineda, J. E. (2014). From Filamentary Networks to Dense Cores in Molecular Clouds: Toward a New Paradigm for Star Formation. In Beuther, H., Klessen, R. S., Dullemond, C. P., and Henning, T., editors, *Protostars and Planets VI*, pages 27–51.

André, P., Men'shchikov, A., Bontemps, S., Könyves, V., Motte, F., Schneider, N., Didelon, P., Minier, V., Saraceno, P., Ward-Thompson, D., di Francesco, J., White, G., Molinari, S., Testi, L., Abergel, A., Griffin, M., Henning, T., Royer, P., Merín, B., Vavrek, R., Attard, M., Arzoumanian, D., Wilson, C. D., Ade, P., Aussel, H., Baluteau, J. P., Benedettini, M., Bernard, J. P., Blommaert, J. A. D. L., Cambrésy, L., Cox, P., di Giorgio, A., Hargrave, P., Hennemann, M., Huang, M., Kirk, J., Krause, O., Launhardt, R., Leeks, S., Le Pennec, J., Li, J. Z., Martin, P. G., Maury, A., Olofsson, G., Omont, A., Peretto, N., Pezzuto, S., Prusti, T., Roussel, H., Russeil, D., Sauvage, M., Sibthorpe, B., Sicilia-Aguilar, A., Spinoglio, L., Waelkens, C., Woodcraft, A., and Zavagno, A. (2010). From filamentary clouds to prestellar cores to the stellar IMF: Initial highlights from the Herschel Gould Belt Survey. , 518:L102.

Armante, M., Gusdorf, A., Louvet, F., Motte, F., Pouteau, Y., Lesaffre, P., Galván-Madrid, R., Dell'Ova, P., Bonfand, M., Nony, T., Brouillet, N., Cunningham, N., Ginsburg, A., Men'shchikov, A., Bontemps, S., Díaz-González, D., Csengeri, T., Fernández-López, M., González, M., Herpin, F., Liu, H. L., Sanhueza, P., Stutz, A. M., and Valeille-Manet, M. (2024). ALMA-IMF. X. The core population in the evolved W33-Main (G012.80) protocluster. , 686:A122.

Bergin, E. A. and Langer, W. D. (1997). Chemical Evolution in Preprotostellar and Protostellar Cores. , 486(1):316–328.

Bergin, E. A. and Tafalla, M. (2007). Cold Dark Clouds: The Initial Conditions for Star Formation. , 45(1):339–396.

Bonfand, M., Csengeri, T., Bontemps, S., Brouillet, N., Motte, F., Louvet, F., Ginsburg, A., Cunningham, N., Galván-Madrid, R., Herpin, F., Wyrowski, F., Valeille-Manet, M., Stutz, A. M., Di Francesco, J., Gusdorf, A., Fernández-López, M., Lefloch, B., Liu, H. L., Sanhueza, P., Álvarez-Gutiérrez, R. H., Olguin, F., Nony, T., Lopez-Sepulcre, A., Dell'Ova, P., Pouteau, Y., Jeff, D., Chen, H. R. V., Armante, M., Towner, A., Bronfman, L., and Kessler, N. (2024). ALMA-IMF. XI. The sample of hot core candidates: A rich population of young high-mass protostars unveiled by the emission of methyl formate. , 687:A163.

Bontemps, S., Motte, F., Csengeri, T., and Schneider, N. (2010). Fragmentation and mass segregation in the massive dense cores of Cygnus X. , 524:A18.

Busquet, G., Estalella, R., Zhang, Q., Viti, S., Palau, A., Ho, P. T. P., and Sánchez-Monge, Á. (2011). N_2H^+ depletion in the massive protostellar cluster AFGL 5142. , 525:A141.

Caselli, P. and Ceccarelli, C. (2012). Our astrochemical heritage. , 20:56.

Caselli, P., Myers, P. C., and Thaddeus, P. (1995). Radio-astronomical Spectroscopy of the Hyperfine Structure of N 2H +. , 455:L77.

Caselli, P., Walmsley, C. M., Zucconi, A., Tafalla, M., Dore, L., and Myers, P. C. (2002). Molecular Ions in L1544. II. The Ionization Degree. , 565(1):344–358.

Cunningham, N., Ginsburg, A., Galván-Madrid, R., Motte, F., Csengeri, T., Stutz, A. M., Fernández-López, M., Álvarez-Gutiérrez, R. H., Armante, M., Baug, T., Bonfand, M., Bontemps, S., Braine, J., Brouillet, N., Busquet, G., Díaz-González, D. J., Di Francesco, J., Gusdorf, A., Herpin, F., Liu, H., López-Sepulcre, A., Louvet, F., Lu, X., Maud, L., Nony, T., Olguin, F. A., Pouteau, Y., Rivera-Soto, R., Sandoval-Garrido, N. A., Sanhueza, P., Tatematsu, K., Towner, A. P. M., and Valeille-Manet, M. (2023). ALMA-IMF. VII. First release of the full spectral line cubes: Core kinematics traced by DCN J = (3−2). , 678:A194.

Dell'Ova, P., Motte, F., Gusdorf, A., Pouteau, Y., Men'shchikov, A., Díaz-González, D., Galván-Madrid, R., Lesaffre, P., Didelon, P., Stutz, A. M., Towner, A. P. M., Marsh, K., Whitworth, A., Armante, M., Bonfand, M., Nony,

T., Valeille-Manet, M., Bontemps, S., Csengeri, T., Cunningham, N., Ginsburg, A., Louvet, F., Álvarez-Gutiérrez, R. H., Brouillet, N., Salinas, J., Sanhueza, P., Nakamura, F., Nguyen Luong, Q., Baug, T., Fernández-López, M., Liu, H. L., and Olguin, F. (2024). ALMA-IMF. XII. Point-process mapping of 15 massive protoclusters. , 687:A217.

Duarte-Cabral, A., Bontemps, S., Motte, F., Hennemann, M., Schneider, N., and André, P. (2013). CO outflows from high-mass Class 0 protostars in Cygnus-X. , 558:A125.

Dunham, M. M., Stutz, A. M., Allen, L. E., Evans, N. J., I., Fischer, W. J., Megeath, S. T., Myers, P. C., Offner, S. S. R., Poteet, C. A., Tobin, J. J., and Vorobyov, E. I. (2014). The Evolution of Protostars: Insights from Ten Years of Infrared Surveys with Spitzer and Herschel. In Beuther, H., Klessen, R. S., Dullemond, C. P., and Henning, T., editors, *Protostars and Planets VI*, pages 195–218.

Dunham, M. M. and Vorobyov, E. I. (2012). Resolving the Luminosity Problem in Low-mass Star Formation. , 747(1):52.

Evans, Neal J., I., Dunham, M. M., Jørgensen, J. K., Enoch, M. L., Merín, B., van Dishoeck, E. F., Alcalá, J. M., Myers, P. C., Stapelfeldt, K. R., Huard, T. L., Allen, L. E., Harvey, P. M., van Kempen, T., Blake, G. A., Koerner, D. W., Mundy, L. G., Padgett, D. L., and Sargent, A. I. (2009). The Spitzer c2d Legacy Results: Star-Formation Rates and Efficiencies; Evolution and Lifetimes. , 181(2):321–350.

Friesen, R. K., Di Francesco, J., Myers, P. C., Belloche, A., Shirley, Y. L., Bourke, T. L., and André, P. (2010). The Initial Conditions of Clustered Star Formation. III. The Deuterium Fractionation of the Ophiuchus B2 Core. , 718(2):666–682.

Furlan, E., Fischer, W. J., Ali, B., Stutz, A. M., Stanke, T., Tobin, J. J., Megeath, S. T., Osorio, M., Hartmann, L., Calvet, N., Poteet, C. A., Booker, J., Manoj, P., Watson, D. M., and Allen, L. (2016). The Herschel Orion Protostar Survey: Spectral Energy Distributions and Fits Using a Grid of Protostellar Models. , 224(1):5.

Galván-Madrid, R., Díaz-González, D. J., Motte, F., Ginsburg, A., Cunningham, N., Menten, K. M., Armante, M., Bonfand, M., Braine, J., Csengeri, T., Dell'Ova, P., Louvet, F., Nony, T., Rivera-Soto, R., Sanhueza, P., Stutz, A. M., Wyrowski, F., Álvarez-Gutiérrez, R. H., Baug, T., Bontemps, S., Bronfman, L., Fernández-López, M., Gusdorf, A., Koley, A., Liu, H.-L., Salinas, J., Towner, A. P. M., and Whitworth, A. P. (2024). ALMA-IMF XIV: Free-Free Templates Derived from H41α and Ionized Gas Content in Fifteen Massive Protoclusters. *arXiv e-prints*, page arXiv:2407.07359.

Galván-Madrid, R., Zhang, Q., Keto, E., Ho, P. T. P., Zapata, L. A., Rodríguez, L. F., Pineda, J. E., and Vázquez-Semadeni, E. (2010). From the Convergence

of Filaments to Disk-outflow Accretion: Massive Star Formation in W33A. , 725(1):17–28.

Ginsburg, A., Csengeri, T., Galván-Madrid, R., Cunningham, N., Álvarez-Gutiérrez, R. H., Baug, T., Bonfand, M., Bontemps, S., Busquet, G., Díaz-González, D. J., Fernández-López, M., Guzmán, A., Herpin, F., Liu, H., López-Sepulcre, A., Louvet, F., Maud, L., Motte, F., Nakamura, F., Nony, T., Olguin, F. A., Pouteau, Y., Sanhueza, P., Stutz, A. M., Towner, A. P. M., ALMA-IMF Consortium, Armante, M., Battersby, C., Bronfman, L., Braine, J., Brouillet, N., Chapillon, E., Di Francesco, J., Gusdorf, A., Izumi, N., Joncour, I., Walker Lu, X., Men'shchikov, A., Menten, K. M., Moraux, E., Molet, J., Mundy, L., Nguyen Luong, Q., Reyes-Reyes, S. D., Robitaille, J., Rosolowsky, E., Sandoval-Garrido, N. A., Svoboda, B., Tatematsu, K., Walker, D. L., Whitworth, A., Wu, B., and Wyrowski, F. (2022a). ALMA-IMF. II. Investigating the origin of stellar masses: Continuum images and data processing. , 662:A9.

Ginsburg, A., Sokolov, V., de Val-Borro, M., Rosolowsky, E., Pineda, J. E., Sipőcz, B. M., and Henshaw, J. D. (2022b). Pyspeckit: A Spectroscopic Analysis and Plotting Package. , 163(6):291.

Gómez, G. C., Walsh, C., and Palau, A. (2022). Different molecular filament widths as tracers of accretion on to filaments. , 513(1):1244–1253.

González Lobos, V. and Stutz, A. M. (2019). Gas velocity structure of the Orion A integral-shaped filament. , 489(4):4771–4782.

Hacar, A., Clark, S. E., Heitsch, F., Kainulainen, J., Panopoulou, G. V., Seifried, D., and Smith, R. (2023). Initial Conditions for Star Formation: a Physical Description of the Filamentary ISM. In Inutsuka, S., Aikawa, Y., Muto, T., Tomida, K., and Tamura, M., editors, *Protostars and Planets VII*, volume 534 of *Astronomical Society of the Pacific Conference Series*, page 153.

Hacar, A., Tafalla, M., Kauffmann, J., and Kovács, A. (2013). Cores, filaments, and bundles: hierarchical core formation in the L1495/B213 Taurus region. , 554:A55.

Haschick, A. D. and Ho, P. T. P. (1983). Formation of OB clusters : W 33 complex. , 267:638–646.

Immer, K., Galván-Madrid, R., König, C., Liu, H. B., and Menten, K. M. (2014). Diversity of chemistry and excitation conditions in the high-mass star forming complex W33. , 572:A63.

Immer, K., Reid, M. J., Menten, K. M., Brunthaler, A., and Dame, T. M. (2013). Trigonometric parallaxes of massive star forming regions: G012.88+0.48 and W33. , 553:A117.

Jessop, N. E. and Ward-Thompson, D. (2000). A far-infrared survey of molecular cloud cores. , 311(1):63–74.

Kainulainen, J., Hacar, A., Alves, J., Beuther, H., Bouy, H., and Tafalla, M. (2016). Gravitational fragmentation caught in the act: the filamentary Musca molecular cloud. , 586:A27.

Kainulainen, J., Stutz, A. M., Stanke, T., Abreu-Vicente, J., Beuther, H., Henning, T., Johnston, K. G., and Megeath, S. T. (2017). Resolving the fragmentation of high line-mass filaments with ALMA: the integral shaped filament in Orion A. , 600:A141.

Kirk, H., Myers, P. C., Bourke, T. L., Gutermuth, R. A., Hedden, A., and Wilson, G. W. (2013). Filamentary Accretion Flows in the Embedded Serpens South Protocluster. , 766(2):115.

Kong, S., Arce, H. G., Maureira, M. J., Caselli, P., Tan, J. C., and Fontani, F. (2019). Widespread Molecular Outflows in the Infrared Dark Cloud G28.37+0.07: Indications of Orthogonal Outflow-filament Alignment. , 874(1):104.

Könyves, V., André, P., Men'shchikov, A., Palmeirim, P., Arzoumanian, D., Schneider, N., Roy, A., Didelon, P., Maury, A., Shimajiri, Y., Di Francesco, J., Bontemps, S., Peretto, N., Benedettini, M., Bernard, J. P., Elia, D., Griffin, M. J., Hill, T., Kirk, J., Ladjelate, B., Marsh, K., Martin, P. G., Motte, F., Nguyên Luong, Q., Pezzuto, S., Roussel, H., Rygl, K. L. J., Sadavoy, S. I., Schisano, E., Spinoglio, L., Ward-Thompson, D., and White, G. J. (2015). A census of dense cores in the Aquila cloud complex: SPIRE/PACS observations from the Herschel Gould Belt survey. , 584:A91.

Ladjelate, B., André, P., Könyves, V., Ward-Thompson, D., Men'shchikov, A., Bracco, A., Palmeirim, P., Roy, A., Shimajiri, Y., Kirk, J. M., Arzoumanian, D., Benedettini, M., Di Francesco, J., Fiorellino, E., Schneider, N., Pezzuto, S., Motte, F., and Herschel Gould Belt Survey Team (2020). The Herschel view of the dense core population in the Ophiuchus molecular cloud. , 638:A74.

Lippok, N., Launhardt, R., Semenov, D., Stutz, A. M., Balog, Z., Henning, T., Krause, O., Linz, H., Nielbock, M., Pavlyuchenkov, Y. N., Schmalzl, M., Schmiedeke, A., and Bieging, J. H. (2013). Gas-phase CO depletion and N_2H^+ abundances in starless cores. , 560:A41.

Liu, H.-L., Tej, A., Liu, T., Sanhueza, P., Qin, S.-L., He, J., Goldsmith, P. F., Garay, G., Pan, S., Morii, K., Li, S., Stutz, A., Tatematsu, K., Xu, F.-W., Bronfman, L., Saha, A., Issac, N., Baug, T., Toth, L. V., Dewangan, L., Wang, K., Zhou, J., Lee, C. W., Yang, D., Luo, A., Shen, X., Zhang, Y., Wu, Y.-F., Ren, Z., Liu, X.-C., Soam, A., Zhang, S., and Luo, Q.-Y. (2023). Evidence of high-mass star formation through multiscale mass accretion in hub-filament-system clouds. , 522(3):3719–3734.

Louvet, F., Sanhueza, P., Stutz, A., Men'shchikov, A., Motte, F., Galván-Madrid, R., Bontemps, S., Pouteau, Y., Ginsburg, A., Csengeri, T., Di Francesco, J., Dell'Ova, P., González, M., Didelon, P., Braine, J., Cunningham, N., Thomasson, B., Lesaffre, P., Hennebelle, P., Bonfand, M., Gusdorf, A., Álvarez-Gutiérrez,

R. H., Nony, T., Busquet, G., Olguin, F., Bronfman, L., Salinas, J., Fernandez-Lopez, M., Moraux, E., Liu, H. L., Lu, X., Huei-Ru, V., Towner, A., Valeille-Manet, M., Brouillet, N., Herpin, F., Lefloch, B., Baug, T., Maud, L., López-Sepulcre, A., and Svoboda, B. (2024). ALMA-IMF: XV. Core mass function in the high-mass star formation regime. , 690:A33.

Megeath, S. T., Gutermuth, R., Muzerolle, J., Kryukova, E., Flaherty, K., Hora, J. L., Allen, L. E., Hartmann, L., Myers, P. C., Pipher, J. L., Stauffer, J., Young, E. T., and Fazio, G. G. (2012). The Spitzer Space Telescope Survey of the Orion A and B Molecular Clouds. I. A Census of Dusty Young Stellar Objects and a Study of Their Mid-infrared Variability. , 144(6):192.

Megeath, S. T., Gutermuth, R., Muzerolle, J., Kryukova, E., Hora, J. L., Allen, L. E., Flaherty, K., Hartmann, L., Myers, P. C., Pipher, J. L., Stauffer, J., Young, E. T., and Fazio, G. G. (2016). The Spitzer Space Telescope Survey of the Orion A and B Molecular Clouds. II. The Spatial Distribution and Demographics of Dusty Young Stellar Objects. , 151(1):5.

Megeath, S. T., Gutermuth, R. A., and Kounkel, M. A. (2022). Low Mass Stars as Tracers of Star and Cluster Formation. , 134(1034):042001.

Merín, B., Jørgensen, J., Spezzi, L., Alcalá, J. M., Evans, Neal J., I., Harvey, P. M., Prusti, T., Chapman, N., Huard, T., van Dishoeck, E. F., and Comerón, F. (2008). The Spitzer c2d Survey of Large, Nearby, Interstellar Clouds. XI. Lupus Observed with IRAC and MIPS. , 177(2):551–583.

Motte, F., Bontemps, S., Csengeri, T., Pouteau, Y., Louvet, F., Stutz, A. M., Cunningham, N., López-Sepulcre, A., Brouillet, N., Galván-Madrid, R., Ginsburg, A., Maud, L., Men'shchikov, A., Nakamura, F., Nony, T., Sanhueza, P., Álvarez-Gutiérrez, R. H., Armante, M., Baug, T., Bonfand, M., Busquet, G., Chapillon, E., Díaz-González, D., Fernández-López, M., Guzmán, A. E., Herpin, F., Liu, H. L., Olguin, F., Towner, A. P. M., Bally, J., Battersby, C., Braine, J., Bronfman, L., Chen, H. R. V., Dell'Ova, P., Di Francesco, J., González, M., Gusdorf, A., Hennebelle, P., Izumi, N., Joncour, I., Lee, Y. N., Lefloch, B., Lesaffre, P., Lu, X., Menten, K. M., Mignon-Risse, R., Molet, J., Moraux, E., Mundy, L., Nguyen Luong, Q., Reyes, N., Reyes Reyes, S. D., Robitaille, J. F., Rosolowsky, E., Sandoval-Garrido, N. A., Schuller, F., Svoboda, B., Tatematsu, K., Thomasson, B., Walker, D., Wu, B., Whitworth, A. P., and Wyrowski, F. (2022). ALMA-IMF. I. Investigating the origin of stellar masses: Introduction to the Large Program and first results. , 662:A8.

Motte, F., Bontemps, S., and Louvet, F. (2018). High-Mass Star and Massive Cluster Formation in the Milky Way. , 56:41–82.

Nony, T., Galván-Madrid, R., Motte, F., Pouteau, Y., Cunningham, N., Louvet, F., Stutz, A. M., Lefloch, B., Bontemps, S., Brouillet, N., Ginsburg, A., Joncour, I., Herpin, F., Sanhueza, P., Csengeri, T., Towner, A. P. M., Bonfand, M., Fernández-López, M., Baug, T., Bronfman, L., Busquet, G., Di Francesco, J., Gusdorf, A., Lu, X., Olguin, F., Valeille-Manet, M., and Whitworth, A. P.

(2023). ALMA-IMF. V. Prestellar and protostellar core populations in the W43 cloud complex. , 674:A75.

Palau, A., Fuente, A., Girart, J. M., Estalella, R., Ho, P. T. P., Sánchez-Monge, Á., Fontani, F., Busquet, G., Commerçon, B., Hennebelle, P., Boissier, J., Zhang, Q., Cesaroni, R., and Zapata, L. A. (2013). Early Stages of Cluster Formation: Fragmentation of Massive Dense Cores down to $<_{\sim}$1000 AU. , 762(2):120.

Peretto, N., Fuller, G. A., André, P., Arzoumanian, D., Rivilla, V. M., Bardeau, S., Duarte Puertas, S., Guzman Fernandez, J. P., Lenfestey, C., Li, G. X., Olguin, F. A., Röck, B. R., de Villiers, H., and Williams, J. (2014). SDC13 infrared dark clouds: Longitudinally collapsing filaments? , 561:A83.

Pouteau, Y., Motte, F., Nony, T., Galván-Madrid, R., Men'shchikov, A., Bontemps, S., Robitaille, J. F., Louvet, F., Ginsburg, A., Herpin, F., López-Sepulcre, A., Dell'Ova, P., Gusdorf, A., Sanhueza, P., Stutz, A. M., Brouillet, N., Thomasson, B., Armante, M., Baug, T., Bonfand, M., Busquet, G., Csengeri, T., Cunningham, N., Fernández-López, M., Liu, H. L., Olguin, F., Towner, A. P. M., Bally, J., Braine, J., Bronfman, L., Joncour, I., González, M., Hennebelle, P., Lu, X., Menten, K. M., Moraux, E., Tatematsu, K., Walker, D., and Whitworth, A. P. (2022). ALMA-IMF. III. Investigating the origin of stellar masses: top-heavy core mass function in the W43-MM2&MM3 mini-starburst. , 664:A26.

Pouteau, Y., Motte, F., Nony, T., González, M., Joncour, I., Robitaille, J. F., Busquet, G., Galván-Madrid, R., Gusdorf, A., Hennebelle, P., Ginsburg, A., Csengeri, T., Sanhueza, P., Dell'Ova, P., Stutz, A. M., Towner, A. P. M., Cunningham, N., Louvet, F., Men'shchikov, A., Fernández-López, M., Schneider, N., Armante, M., Bally, J., Baug, T., Bonfand, M., Bontemps, S., Bronfman, L., Brouillet, N., Díaz-González, D., Herpin, F., Lefloch, B., Liu, H. L., Lu, X., Nakamura, F., Nguyen-Luong, Q., Olguin, F., Tatematsu, K., and Valeille-Manet, M. (2023). ALMA-IMF. VI. Investigating the origin of stellar masses: Core mass function evolution in the W43-MM2&MM3 mini-starburst. , 674:A76.

Punanova, A., Caselli, P., Pon, A., Belloche, A., and André, P. (2016). Deuterium fractionation in the Ophiuchus molecular cloud. , 587:A118.

Redaelli, E., Bizzocchi, L., Caselli, P., Sipilä, O., Lattanzi, V., Giuliano, B. M., and Spezzano, S. (2019). High-sensitivity maps of molecular ions in L1544. I. Deuteration of N_2H^+ and HCO^+ and primary evidence of N_2D^+ depletion. , 629:A15.

Reyes-Reyes, S. D., Stutz, A. M., Megeath, S. T., Xu, F., Álvarez-Gutiérrez, R. H., Sandoval-Garrido, N., and Liu, H. L. (2024). Benchmarking the IRDC G351.77-0.53: Gaia DR3 distance, mass distribution, and star formation content. , 529(3):2220–2233.

Sandoval-Garrido, N. A., Stutz, A. M., Álvarez-Gutiérrez, R. H., Galván-Madrid, R., Motte, F., Ginsburg, A., Cunningham, N., Reyes-Reyes, S., Redaelli, E., Bonfand, M., Salinas, J., Koley, A., Braine, J., Bronfman, L., Busquet, G.,

Csengeri, T., Di Francesco, J., Fernández-López, M., Garcia, P., Gusdorf, A., Liu, H. L., and Sanhueza, P. (2024). ALMA-IMF XVIII: The assembly of a star cluster: Dense N_2H^+ (1-0) kinematics in the massive G351.77 protocluster. *arXiv e-prints*, page arXiv:2410.09843.

Schneider, N., Csengeri, T., Hennemann, M., Motte, F., Didelon, P., Federrath, C., Bontemps, S., Di Francesco, J., Arzoumanian, D., Minier, V., André, P., Hill, T., Zavagno, A., Nguyen-Luong, Q., Attard, M., Bernard, J. P., Elia, D., Fallscheer, C., Griffin, M., Kirk, J., Klessen, R., Könyves, V., Martin, P., Men'shchikov, A., Palmeirim, P., Peretto, N., Pestalozzi, M., Russeil, D., Sadavoy, S., Sousbie, T., Testi, L., Tremblin, P., Ward-Thompson, D., and White, G. (2012). Cluster-formation in the Rosette molecular cloud at the junctions of filaments. , 540:L11.

Shirley, Y. L. (2015). The Critical Density and the Effective Excitation Density of Commonly Observed Molecular Dense Gas Tracers. , 127(949):299.

Stutz, A. M. (2018). Slingshot mechanism for clusters: Gas density regulates star density in the Orion Nebula Cluster (M42). , 473(4):4890–4899.

Stutz, A. M., Gonzalez-Lobos, V., and Gould, A. (2018). Gaia: Orion's Integral Shaped Filament is a Standing Wave. *arXiv e-prints*, page arXiv:1807.11496.

Stutz, A. M. and Gould, A. (2016). Slingshot mechanism in Orion: Kinematic evidence for ejection of protostars by filaments. , 590:A2.

Tafalla, M., Santiago, J., Johnstone, D., and Bachiller, R. (2004). A highly collimated, extremely high velocity outflow in Taurus. , 423:L21–L24.

Tafalla, M., Usero, A., and Hacar, A. (2021). Characterizing the line emission from molecular clouds. Stratified random sampling of the Perseus cloud. , 646:A97.

Tanaka, T., Nakamura, F., Awazu, Y., Shimajiri, Y., Sugitani, K., Onishi, T., Kawabe, R., Yoshida, H., and Higuchi, A. E. (2013). The Dynamical State of the Serpens South Filamentary Infrared Dark Cloud. , 778(1):34.

Tatematsu, K., Kandori, R., Umemoto, T., and Sekimoto, Y. (2008). N_2H^+ and HC_3N Observations of the Orion A Cloud. , 60:407.

Thaddeus, P. and Turner, B. E. (1975). Confirmation of interstellar N_2H^+. , 201:L25–L26.

Tobin, J. J., Bergin, E. A., Hartmann, L., Lee, J.-E., Maret, S., Myers, P. C., Looney, L. W., Chiang, H.-F., and Friesen, R. (2013). Resolved Depletion Zones and Spatial Differentiation of N_2H^+ and N_2D^+. , 765(1):18.

Towner, A. P. M., Ginsburg, A., Dell'Ova, P., Gusdorf, A., Bontemps, S., Csengeri, T., Galván-Madrid, R., Louvet, F. K., Motte, F., Sanhueza, P., Stutz, A. M., Bally, J., Baug, T., Chen, H. R. V., Cunningham, N., Fernández-López, M., Liu, H. L., Lu, X., Nony, T., Valeille-Manet, M., Wu, B., Álvarez-Gutiérrez, R. H., Bonfand, M., Di Francesco, J., Nguyen-Luong, Q., Olguin, F., and Whitworth,

A. P. (2024). ALMA-IMF. IX. Catalog and Physical Properties of 315 SiO Outflow Candidates in 15 Massive Protoclusters. , 960(1):48.

Vigren, E., Zhaunerchyk, V., Hamberg, M., Kaminska, M., Semaniak, J., Ugglas, M. a., Larsson, M., Thomas, R. D., and Geppert, W. D. (2012). Reassessment of the Dissociative Recombination of N_2H^+ at CRYRING. , 757(1):34.

Williams, G. M. (2018). *The evolution and formation of the SDC13 Infrared Dark Cloud hub filament system*. PhD thesis, Cardiff University, UK.

Xie, J., Li, J., Wang, J., Liu, S., Yang, K., Quan, D., Zheng, S., Li, Y., Wu, J., Duan, Y., and Li, D. (2023). Imaging Molecular Outflow in Massive Star-forming Regions with HNCO Lines. , 949(2):89.

Xu, F.-W., Wang, K., Liu, T., Goldsmith, P. F., Zhang, Q., Juvela, M., Liu, H.-L., Qin, S.-L., Li, G.-X., Tej, A., Garay, G., Bronfman, L., Li, S., Wu, Y.-F., Gómez, G. C., Vázquez-Semadeni, E., Tatematsu, K., Ren, Z., Zhang, Y., Toth, L. V., Liu, X., Yue, N., Zhang, S., Baug, T., Issac, N., Stutz, A. M., Liu, M., Fuller, G. A., Tang, M., Zhang, C., Dewangan, L., Lee, C. W., Zhou, J., Xie, J., Jiao, W., Wang, C., Liu, R., Luo, Q., Soam, A., and Eswaraiah, C. (2023). ATOMS: ALMA Three-millimeter Observations of Massive Star-forming regions - XV. Steady accretion from global collapse to core feeding in massive hub-filament system SDC335. , 520(3):3259–3285.

Yu, N., Wang, J.-J., and Xu, J.-L. (2019). Chemical evolution of HC_3N in dense molecular clouds. , 489(4):4497–4512.

Yu, N.-P., Xu, J.-L., Wang, J.-J., and Liu, X.-L. (2018). Chemical Evolution of N_2H^+ in Six Massive Star-forming Regions. , 865(2):135.

Yu, N.-P., Xu, J.-L., Zhang, C.-P., Jiang, P., Liu, X.-L., and Wang, J.-J. (2022). Physical and Chemical Properties of the Molecular Gas Associated with the Mid-infrared Bubble S156. , 928(1):83.

Zhou, J.-W., Liu, T., Evans, N. J., Garay, G., Goldsmith, P. F., Gómez, G. C., Vázquez-Semadeni, E., Liu, H.-L., Stutz, A. M., Wang, K., Juvela, M., He, J., Li, D., Bronfman, L., Liu, X., Xu, F.-W., Tej, A., Dewangan, L. K., Li, S., Zhang, S., Zhang, C., Ren, Z., Tatematsu, K., Shing Li, P., Won Lee, C., Baug, T., Qin, S.-L., Wu, Y., Peng, Y., Zhang, Y., Liu, R., Luo, Q.-Y., Ge, J., Saha, A., Chakali, E., Zhang, Q., Kim, K.-T., Ristorcelli, I., Shen, Z.-Q., and Li, J.-Z. (2022). ATOMS: ALMA Three-millimeter Observations of Massive Star-forming regions - XI. From inflow to infall in hub-filament systems. , 514(4):6038–6052.

A1 N_2H^+ (1−0) line fitting: one and two velocity components

In this appendix, we describe the data preparation steps prior to line fitting, including S/N analysis and input parameter selection. We also characterize the output modeling parameters and associated uncertainties, identifying the velocity structures used in the above analysis.

A1.1 Data preparation

Before fitting, we evaluate the robustness of the N_2H^+ data cube by examining negative bowls and noise. We find the most negative values concentrated in a central and compact area of G012. Next, we construct an S/N map to locate the most reliable values. The noise is measured by identifying emission-free channels within the velocity ranges of $12\,\mathrm{km\,s^{-1}}$ to $20\,\mathrm{km\,s^{-1}}$ and $49\,\mathrm{km\,s^{-1}}$ to $61\,\mathrm{km\,s^{-1}}$, defining the noise as the standard deviation over these channels and the signal as the maximum intensity per pixel. We apply an S/N threshold of 12 to retain the majority of the N_2H^+ structure while excluding unreliable spectra that cannot be accurately fitted.

We construct the preliminary moment 0 and 1 maps, using the full line for the integrated intensity map and the isolated component for the mean velocity (see Álvarez-Gutiérrez et al., 2024, for details on isolated component identification). The integrated intensity map (right panel in Fig. 1.0.1) reveals prominent N_2H^+ structures along two main filaments and shows a disrupted central morphology in G012. The moment 1 map reveals a velocity gradient perpendicular to the R1 filament ridgeline (discussed in Sec. 4.1), and regions with high and spread velocities in the central area, potentially related to multiple velocity components (see below).

A1.2 Choosing input parameters

To model the N_2H^+ data, we used the *specfit* fitting tool based on the built-in *n2hp_vtau* fitter. The *specfit* task requires the following input values:

1. *fittype*: specifies the model type and requires the number of velocity components and model parameters,

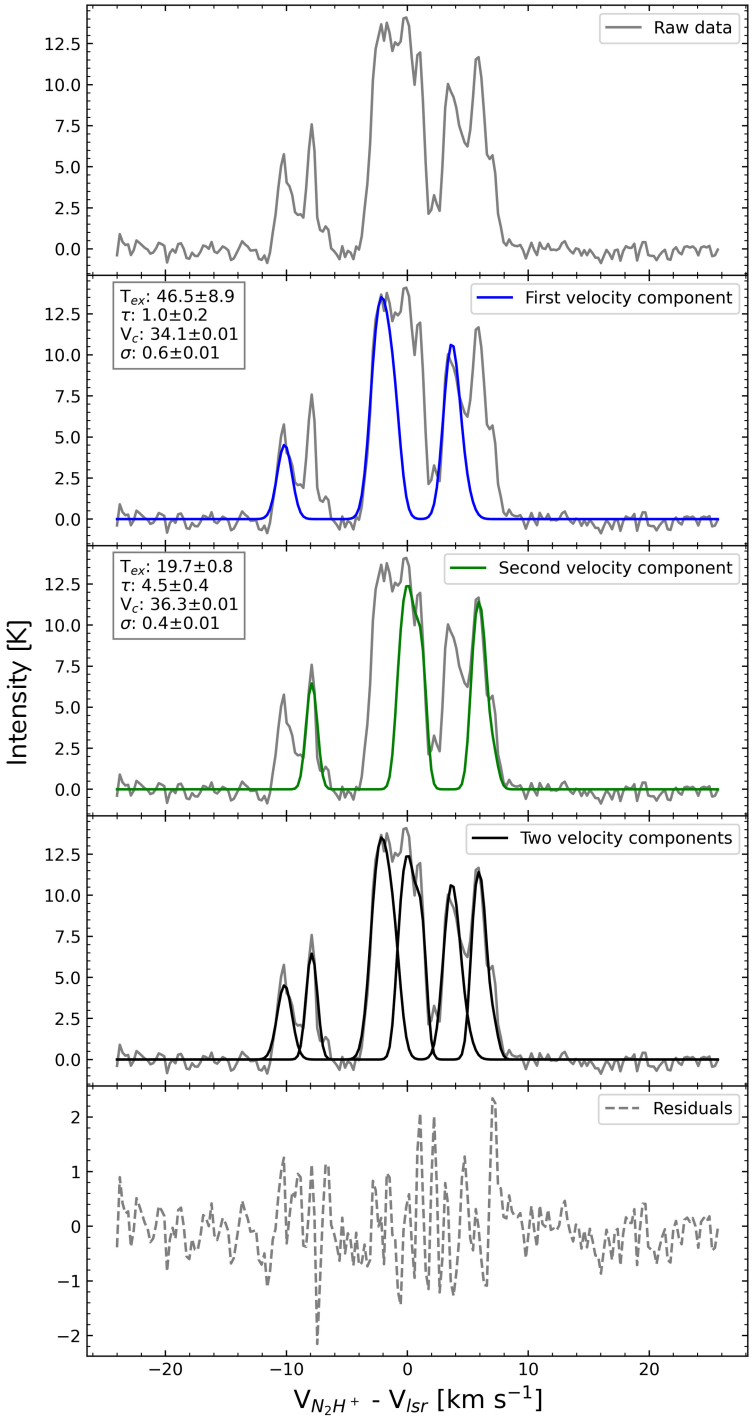

Figure A1.1: N_2H^+ two velocity component fitting example: The panels, from top to bottom, display the raw data (grey curve), the first velocity component (blue curve) overlaid on the raw data, the second velocity component (green curve) overlaid on the raw data, the total model (black curve) fitted to the raw data, and the residuals of the model (grey dashed curve). The `PySpecKit` parameters for both the first and second velocity components are shown in each respective panel.

2. *guesses*: initial model parameter values (only applied to the first pixel fit),
3. *limits*: lower and upper parameter bounds; used across all pixels via the Levenberg-Marquardt algorithm, optimizing the χ^2 function,
4. *limited*: applies or disregards the *limits* defined above,
5. *errmap*: the error map, calculated as the standard deviation in the noise channels (see above),
6. *signal_cut*: defines the signal lower limit for the modeling, where $S/N > signal\_cut$, and
7. *start_from_point*: the initial pixel for fitting.

We test models with one and two velocity components, using four main parameters: the excitation temperature (T_{ex}), optical depth (τ), velocity centroid (V_c), and velocity dispersion (σ). For the initial *guesses* and *limits*, we select values based on the preliminary moment maps described above. The *start_from_point* is chosen as a pixel with high S/N and a well-defined spectrum. Testing various *signal_cut* values confirms that pixels below an S/N of 12 yield poor fits or large uncertainties in critical parameters like radial velocities errors. The input parameters for one- and two-component fits are listed in Table A1.1.

Table A1.1: Starting guesses for spectral fitting

Parameters	$T_{ext}(1)$ [K]	$\tau(1)$	$V_c(1)$ [km s^{-1}]	$\sigma(1)$ [km s^{-1}]	$T_{ext}(2)$ [K]	$\tau(2)$	$V_c(2)$ [km s^{-1}]	$\sigma(2)$ [km s^{-1}]
One velocity component								
Guesses	31.3	3.8	37	0.78	—	—	—	—
Limits	(2.8, 150)	(0.001, 10)	(25, 45)	(0.23, 5)	—	—	—	—
Limited	(T,T)	(T,F)	(T,T)	(T,F)	—	—	—	—
Two velocity components								
Guesses	15	1	33	1.4	20	3	37	0.47
Limits	(2.8, 150)	(0.001, 10)	(25, 45)	(0.23, 5)	(2.8, 150)	(0.001, 10)	(25, 45)	(0.23, 5)
Limited	(T,T)	(T,F)	(T,T)	(T,F)	(T,T)	(T,F)	(T,T)	(T,F)

A1.3 Output parameters and dependencies

`PySpecKit` creates a cube containing the best-fit parameters (T_{ex}, τ, V_c, and σ) and their associated errors for each spectrum and velocity component. We then

obtain an N_2H^+ modeled cube using these parameters and we separate the FVC and SVC into their own cubes.

To assess potential dependencies of certain parameters on our results, we analyze the two most prominent and well-defined N_2H^+ filaments (R1 & R2 in Fig. 1.0.1). We first investigate the *start_pixel* parameter by keeping all other input parameters constant. We perform 716 tests for region R1 and 576 tests for region R2, where each *start_pixel* corresponds to a pixel within our test sub-regions. Our results indicate that parameters and uncertainties are independent of the initial pixel. In addition, we observe that it is necessary to change the starting pixel when adjusting multiple velocity components and respective initial guesses. This change should be to a pixel that exhibits a spectrum where the number of components are well resolved. Furthermore, we test different limits for the parameters ranges in both sub-regions and evaluate their impact on the fitting. We conclude that our selected range is sufficiently wide to avoid biasing the results.

A1.4 Output cleaning

With this modeling approach certain fitted spectrum may yield poor fits due the data being too noisy or having a different number of velocity components. Therefore, it is crucial to properly identify the number of velocity component for each spectrum and review the quality of the associated fitting parameters and errors.

We analyze the error distribution of the four fitted parameters with the goal of accurately describe the kinematics of the G012 N_2H^+ data. We find that errors associated to the centroid and dispersion velocity determination are mostly distributed under $0.3\,\mathrm{km\,s^{-1}}$, with only 5 pixels and 26 pixels exceeding this value, respectively. This is a conservative value relative to the N_2H^+ velocity resolution (slightly less than two velocity channels), therefore, we adopt this value as the maximum allowed error to constrain the V_c and σ errors that we consider associated with a well-fitting spectrum. Additionally, we note that in 184 fits their uncertainties in σ are equal to $0\,\mathrm{km\,s^{-1}}$. This issue occurs when the value associated to the best fit model is one of the limits of the parameter's range. This issue indicates that these fits require a more in depth revision, possibly being better adjusted with more than one velocity component.

The parameter τ is challenging to constrain due to its potential to be infinitely large. In consequence, we set a mask based on the error ratios, using $\frac{\tau}{e(\tau)} > 1$, where $e(\tau)$ is the associated error of τ. Overall, large values of τ are associated with large errors, and a top-flat issue on the spectrum. Therefore, we removed from the model all pixels outside the mask ($\sim$860 pixels). We found the τ values preferably below 25.

For the temperature parameter, we observed that optically thin pixels ($\tau < 1$) yield temperature values at the input upper limit with uncertainties equal to 0 K. However, the temperature parameter does not significantly affect the spectral profiles, even when temperatures reach their extreme values in optically thin pixels. Therefore, to ensure that the cleaning prioritizes accurate the velocity estimates at the initial steps, we not constrain and retain the original T_{ex} output values from the line-fitting, until the column density estimation in Sec. 3.3.

We review the spectra excluded based on the all above criteria, finding that rejected spectra are often associated with multiple velocity components. These initial considerations may be insufficient to detect pixels with multiple velocity components, particularly when two components are difficult to resolve within a single spectrum. To address this, we refit the entire cube with two velocity components, checking whether this approach improves the fit for the spectra within and outside the previously established limits.

For spectra that exhibit only one velocity component, fitting two components often yields suboptimal fits for either the first (bluest) or second (reddest) velocity component. In these cases, we retain the values from the one component fitting, where parameter uncertainties are low and the fit quality is satisfactory (as described above).

Our results show that poor fits in the two velocity components model are associated to high uncertainties, over $0.3\,\mathrm{km\,s^{-1}}$ in velocities errors ($\sim$15 % pixels over this upper limit), larger τ errors relative to their values ($\sim$30 % pixels), parameters with zero values (11 % of pixels), and high τ values. In addition, we set a τ upper limit of 100 for each velocity component, with 52 pixels over.

In total, we obtain $\sim$15,000 spectra with a well defined model for one ($\sim$45%) or two ($\sim$55%) velocity components. Two velocity components are spacially distributed in the whole region, without a prefered location, but with a slight

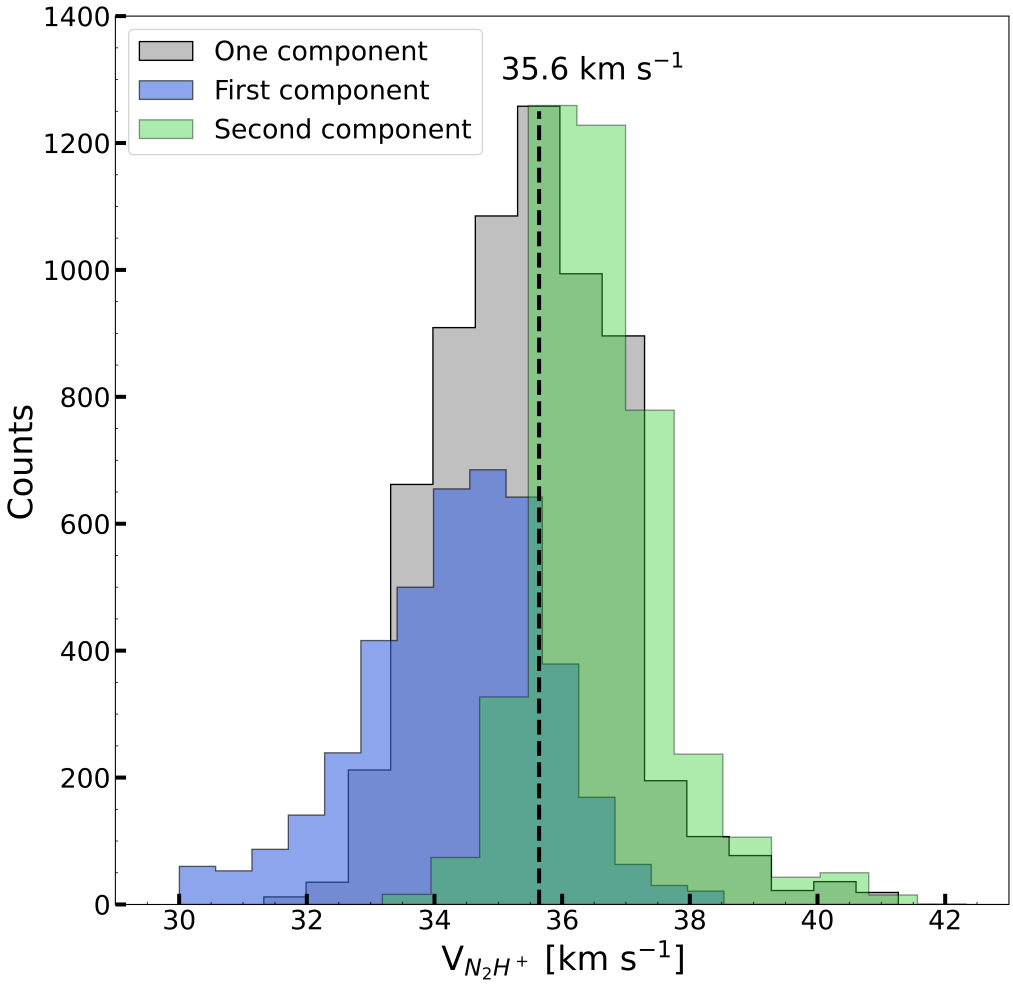

Figure A1.2: Histograms of the velocity distributions for single- (grey) and two-component (blue and green) velocity fits to the spectra (see text). The black dashed line shows the velocity boundary, at 35.6 km s^{-1}, used to distribute one velocity component fits in the merged model cube.

concentration in the R2 filament and in regions with large σ values.

A1.5 Model cube merging

We obtain the final modeled cube by merging the fits with single and double velocity component. To carry out this step we follow a similar method than the one performed by Sandoval-Garrido et al. (2024).

To define a limit between the two velocity components, we calculate the midpoint based on their mean values and standard deviations. Specifically, we take the average of the upper boundary of the first component (mean plus one standard

deviation) and the lower boundary of the second component (mean minus one standard deviation).

$$\text{limit} = \frac{\langle V_{c,1} \rangle + \text{std}(V_{c,1}) + \langle V_{c,2} \rangle - \text{std}(V_{c,2})}{2} \rightarrow 35.6 \text{ km s}^{-1}. \quad \text{(A1.1)}$$

Here $V_{c,1}$ and $V_{c,2}$ correspond to the velocity center parameter of the first (bluest) and second (reddest) velocity component from the double component model, respectively. This approach ensures the limit reflects a balanced division between the two velocity distributions observed in the histogram in Figure A1.2, resulting in a velocity boundary of $35.6\,\text{km}\,\text{s}^{-1}$.

This limit allows us to classify one velocity component into either the first (FVC) or second (SVC) velocity component group. Specifically, components below $35.6\,\text{km}\,\text{s}^{-1}$ ($\sim$ 3,535 pixels) are assigned to the FVC, while those above ($\sim$ 2,984 pixels) are assigned to the SVC, resulting in two new velocity structures: 7,675 pixels in the FVC and 7,124 pixels in the SVC.

A1.6 Complementary tracers line fitting

For other tracers not previously modeled (DCN, H41α, and SiO), we apply a simple Gaussian model using `PySpecKit`. The one Gaussian model requires three input parameters: amplitude (Amp), velocity centroid (V_c), and velocity dispersion (σ), with initial guesses based on moment map values for each spectrum. Since we used a simple model and the computational time required is low, we unlimited the parameter ranges.

In addition, we apply S/N values for each region as *signal_cut* parameter fitting. We determine the S/N for each tracer by measuring the peak intensity for each spectrum and dividing it by their root-mean-square (RMS), estimated using emission-free channels (values reported in Table 2.2.1).

A2 Data alignment

We applied an alignment process to perform different estimates throughout the above sections. For instance, in Sec. 4.1, we aligned the filaments relative to the peak integrated intensity as a function of the filament's length to estimate average velocity gradients, and in Sec. 4.2, we aligned the filament mass map based on

the column density distributions.

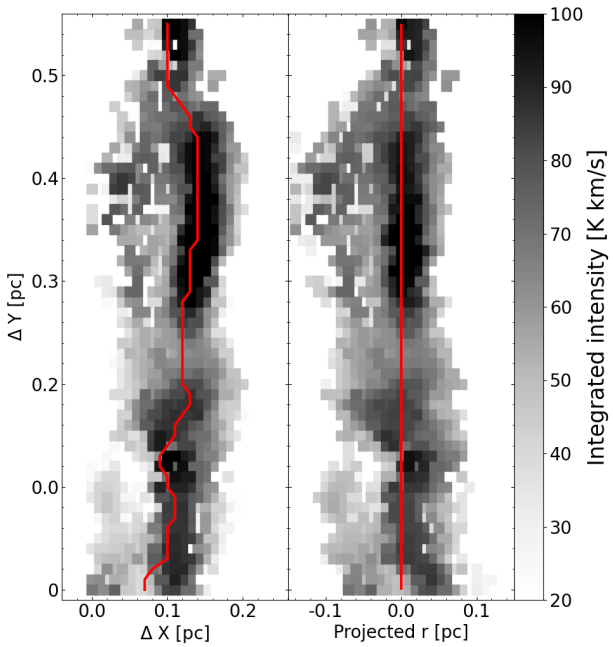

Figure A2.1: Example of the R1 filament alignment relative to the integrated intensity moment map. *Left panel:* Integrated intensity map of the FVC in the R1 region. The red line represent the rigdeline estimated based on the integrated intensity peak along to the filament. The X and Y axis represent the R1 length and width in units of pc. *Right panel:* Integrated intensity map aligned respect to the rigdeline. The X axis represent the projected radius result of the alignment process.

Below, we describe the alignment process for the first case (see Figure A2.1), although the same method can be used to align any dataset to a filament:

1. Map rotation: First, we spatially rotate the N_2H^+ maps (including the integrated intensity, velocity center, and any other maps involved in the procedure) to align the main filaments in the region along the vertical axis (see Figure 3.2.1, upper-left panel as reference).

2. Ridgeline estimation: We then estimated the ridgeline based on the total integrated intensity map of N_2H^+. Specifically, we defined a custom function that accumulates the peak intensity values along the y-axis, helping to trace the integrated intensity spine of the filament (red line in Figure A2.1). The function was applied separately to the R1 and R2 filaments to track their ridgelines individually.

3. Ridgeline smoothing: We used a one-dimensional uniform filter from the `scipy.ndimage` library to smooth the ridgeline. Specifically, we smooth the x-axis of the rigdeline, using a window size of 1 pixel (the same window size was used to align filaments with respect to the column density). This step is relevant to reduce any sharp fluctuations in the ridgeline and create a smoother, more accurate representation of the filament's path.

4. Visualization and analysis: We align the different maps to the smoothed rigdeline (see Figure A2.1, right panel), this alignment allowed us to transform the x-axis into projected radius, facilitating a more refined analysis of velocity and mass profiles.

A3 Mass validaton

In order to validate our mass selection for the line-mass profiles (Sec. 4.2) we compare the mass distribution obtained from the H_2 column density map (Dell'Ova et al., 2024) and the one estimated from N_2H^+ in Sec. 3.3. We select a small and elongated region inside the R2 filament, which well detected in both mass maps, of lenght and width of 0.4 pc and 0.03 pc, respectively.

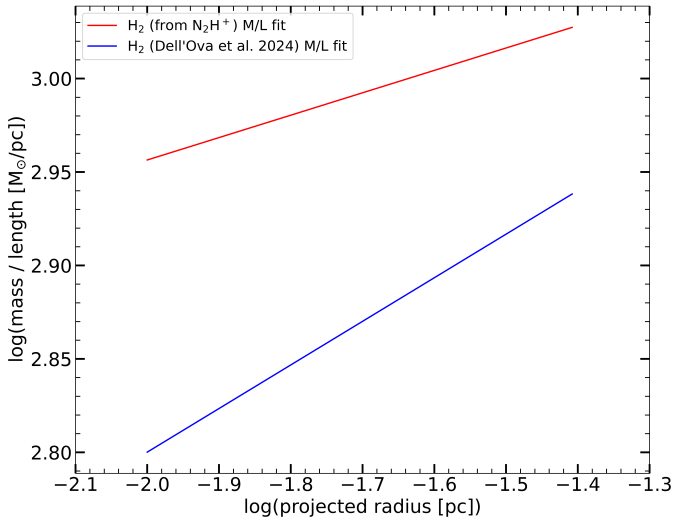

Figure A3.1: Mass over length profile of the selected region for the mass validation step. Red line represents the resulting profile considering H_2 mass estimated in Sec. 4.3, while blue line shows the final profile considering H_2 mass from the column density estimated in Dell'Ova et al. (2024).

We aligned the filament mass to estimate and compare the cumulative mass

distribution within the test region. The cumulative mass distributions appear to be similar following a linear profile but varied slightly in mass values ($\Delta M \sim 300\,M_\odot$). Given the uniform and linear nature of both distributions, we estimated the M/L profiles in the region following the approach presented in Sec. 4.2.

We find minor differences in the inclination of both profiles, as well as the expected difference in the normalization constant. In Fig. A3.1, we present both resulting profiles. Additionally, we estimated the normalization constants of the apparent volume density (Eq. 4.2.3), gravitational potential (Eq. 4.2.4), and gravitational acceleration (Eq. 4.2.5) using both mass distributions. We observed an average difference of 35 % in the line-mass profile parameters and associated metrics.

Considering the small differences between both distributions in a delimited region, and the necessity to improve the mass distribution profile in the R1 filament for the M/L analisis, we choose the total H_2 mass (M_{tot}) map estimated through the N_2H^+ data to the analysis described above in Sec. 4.2.

Using M_{tot}, we obtain a cumulative mass profile in the R1 filament almost linear at different projected radius, considering a filament length of 0.6 pc (see Fig. A3.2)

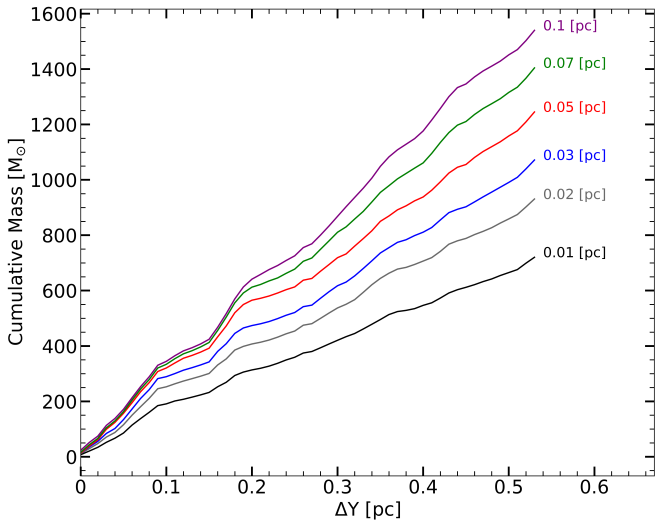

Figure A3.2: Example of cumulative mass profile in the R1 filament. Color curves highlights cumulative mass measurements at different filament radius. Profiles show a linear trend of the cumulative mass along the filament.

A4 Cores tables

Table A4.1: Cores velocities detected in this study I.

DCN and N_2H^+ detected sources

ID[1]	RA	DEC	F(A) [″]	F(B) [″]	PA [deg]	Vel[2] [km/s]	Δ(V)[3] [km/s]
6	273.5557352	-17.9151274	6.80	5.90	141.5	34.5 ± 0.030	+0.08
10	273.5561448	-17.9288124	7.20	4.80	161.5	38.5 ± 0.131	+2.21
15	273.5595282	-17.9203648	14.7	11.7	209.6	34.5 ± 0.064	+0.81
20	273.5585587	-17.9208742	25.9	19.9	138.5	35.2 ± 0.029	+0.29
21	273.5581258	-17.9329013	12.2	10.9	217.1	36.2 ± 0.015	-1.60
24	273.5420287	-17.9327274	10.5	6.60	146.6	36.8 ± 0.064	+0.27
27	273.5587301	-17.9276784	9.10	6.50	172.6	34.8 ± 0.098	-0.18
28	273.5574005	-17.9281480	7.90	4.90	147.4	35.5 ± 0.068	-0.53
35	273.5621830	-17.9302229	23.7	15.1	211.8	35.5 ± 0.005	+0.31
38	273.5511506	-17.9252426	12.5	7.00	128.8	34.5 ± 0.001	-1.42
45	273.5614832	-17.9294106	12.0	8.40	207.1	34.8 ± 0.050	-0.06
49	273.5512430	-17.9221040	7.60	4.80	131.6	34.5 ± 0.022	-1.35
51	273.5456695	-17.9286524	7.40	6.90	144.9	37.5 ± 0.029	+0.29
53	273.5559769	-17.9272312	8.40	5.70	171.6	35.8 ± 0.039	-4.85
55	273.5585399	-17.9322517	9.00	8.80	233.3	35.8 ± 0.087	-2.78
63	273.5559545	-17.9280031	8.50	7.70	175.6	34.8 ± 0.081	-1.01
72	273.5559098	-17.9210339	11.3	7.50	186.2	34.5 ± 0.055	-0.85
80	273.5551376	-17.9282374	8.20	7.20	187.7	36.2 ± 0.026	+0.27
82	273.5541355	-17.9372087	14.1	12.0	173.6	37.2 ± 0.014	+0.94
84	273.5466969	-17.9270489	6.40	4.80	149.7	38.5 ± 0.076	+0.61
87	273.5661498	-17.9243080	7.90	6.40	140.5	35.2 ± 0.017	+0.09
92	273.5644636	-17.9275000	11.4	9.20	140.4	35.5 ± 0.029	+0.47
94	273.5573333	-17.9209924	9.30	5.80	165.6	33.1 ± 0.036	-1.65
96	273.5538282	-17.9203791	15.8	11.2	155.9	36.5 ± 0.056	+0.24
97	273.5534924	-17.9302818	7.20	5.00	154.1	36.5 ± 0.054	+0.71
101	273.5578973	-17.9200468	10.5	8.00	93.50	35.8 ± 0.035	+0.15

(1) We conserve the core ID from Armante et al. (2024) for reference. (2) Centroid velocity estimated trhought the DCN model. (3) V_{DCN} - $V_{N_2H^+}$, positive and negative symbols indicate if the N_2H^+ velocity is blueshifted or redshifted relative to the DCN core velocities.

Table A4.2: Cores velocities detected in this study II.

N_2H^+ detected sources

ID[1]	RA	DEC	F(A) [″]	F(B) [″]	PA [deg]	Vel[2] [km/s]	Δ(V)[3] [km/s]
4	273.5481868	-17.9458387	7.50	5.00	179.0	35.2* ± 0.009	—
9	273.5541976	-17.9141605	7.40	4.40	166.3	33.2 ± 0.010	—
30	273.5472394	-17.9220959	10.0	9.00	178.6	36.4 ± 0.075	—
31	273.5714747	-17.9249529	6.30	4.10	159.5	35.7 ± 0.005	—
47	273.5573736	-17.9253241	7.70	5.90	169.2	36.8 ± 0.047	—
48	273.5599387	-17.9247874	11.2	7.80	133.0	37.8 ± 0.066	—
54	273.5741063	-17.9183977	6.40	5.00	147.4	36.1 ± 0.012	—
66	273.5574878	-17.9319110	9.30	8.30	246.9	38.7 ± 0.021	—
68	273.5655452	-17.9186858	14.4	12.7	235.1	36.4 ± 0.040	—
70	273.5425468	-17.9318786	10.4	7.20	254.2	37.1 ± 0.006	—
71	273.5596700	-17.9235735	10.8	6.60	176.5	38.2 ± 0.055	—
75	273.5384638	-17.9342166	6.20	5.00	140.1	36.8 ± 0.009	—
76	273.5562608	-17.9398390	21.8	18.2	184.3	35.7 ± 0.015	—
77	273.5402299	-17.9333798	8.70	7.10	121.0	36.6 ± 0.006	—
81	273.5453666	-17.9406316	7.10	6.00	246.7	35.7 ± 0.014	—
83	273.5609797	-17.9336253	10.5	7.00	182.6	35.5 ± 0.056	—
86	273.5612818	-17.9299304	9.30	6.60	192.0	34.8 ± 0.049	—
88	273.5693683	-17.9265363	20.1	14.8	97.12	34.3 ± 0.031	—
90	273.5455200	-17.9412705	9.40	7.20	202.1	35.2 ± 0.013	—
93	273.5569036	-17.9273685	7.90	5.60	161.1	36.8 ± 0.050	—
95	273.5437775	-17.9373519	7.50	6.10	239.4	36.1 ± 0.007	—
98	273.5605095	-17.9290040	10.6	8.60	121.9	34.3 ± 0.031	—
DCN detected sources							
79	273.5576220	-17.9229346	8.90	5.80	179.1	37.2 ± 0.030	—
85	273.5636654	-17.9250109	8.30	3.40	140.4	34.8 ± 0.100	—
100	273.5529552	-17.9256818	7.60	4.60	105.0	35.8 ± 0.030	—

(1) We conserve the core ID from Armante et al. (2024) for reference. (2) Centroid velocity estimated trhought DCN model. (3) V_{DCN} - $V_{N_2H^+}$, positive and negative symbols indicate if the N_2H^+ velocity is blueshifted or redshifted relative to the DCN core velocities. (*) For cores without DCN emmision we used N_2H^+ velocity center (and associated uncertainties) extracted from the `PySpecKit` line-fitting.

Table A4.3: N_2H^+ velocities for DCN core catalog by Cunningham et al. (2023)

ID	RA	DEC	F(A) [″]	F(B) [″]	PA [deg]	Vel[1] [km/s]	Δ(V)[2] [km/s]
1.0	273.5493292	-17.9256817	1.60	1.17	57.00	37.11 ± 0.05	+1.36
3.0	273.5573504	-17.9225106	1.84	1.52	8.000	36.02 ± 0.04	-0.24
4.0	273.5444266	-17.9375329	1.41	1.09	91.00	36.16 ± 0.08	+0.66
6.0	273.5531484	-17.9208183	1.59	1.11	54.00	32.60 ± 0.12	-3.80
8.0	273.5486150	-17.9262103	2.35	1.54	69.00	36.60 ± 0.03	+0.10
11.0	273.5547682	-17.9278997	1.72	1.42	76.00	35.81 ± 0.03	+0.32
12.0	273.5444858	-17.9302895	1.50	1.37	71.00	36.87 ± 0.04	+0.07
13.0	273.5484365	-17.9412478	1.75	1.54	17.00	35.40 ± 0.06	+0.60
16.0	273.5526754	-17.9285675	1.35	1.07	66.00	33.85 ± 0.04	-0.43
19.0	273.5561582	-17.9212927	1.78	1.46	176.0	34.77 ± 0.06	-0.92
20.0	273.5569282	-17.9233073	1.82	1.27	40.00	36.15 ± 0.07	—
22.0	273.5661028	-17.9234199	1.56	1.18	54.00	35.46 ± 0.03	+0.64
23.0	273.5464417	-17.9286205	1.68	1.35	61.00	36.98 ± 0.01	+0.25
24.0	273.5689656	-17.9390182	2.10	1.31	67.00	37.33 ± 0.09	+0.51
25.0	273.5690243	-17.9247231	1.85	1.23	90.00	36.08 ± 0.03	+0.39
27.0	273.5561592	-17.9348499	1.97	1.82	171.0	37.53 ± 0.03	+0.73
29.0	273.5516652	-17.9189507	1.91	1.67	112.0	35.86 ± 0.07	+0.37
30.0	273.5576077	-17.9311763	1.68	1.49	15.00	40.03 ± 0.07	+0.90
31.0	273.5676865	-17.9204887	2.18	1.55	158.0	33.48 ± 0.05	-5.58
32.0	273.5470383	-17.9333909	1.60	1.32	29.00	35.39 ± 0.08	+0.59
33.0	273.5581592	-17.9252346	2.16	1.68	25.00	35.28 ± 0.03	-1.79
34.0	273.5465089	-17.9276804	1.63	1.42	37.00	37.66 ± 0.02	+0.47
36.0	273.5569394	-17.9239001	1.71	1.45	67.00	35.79 ± 0.04	—
39.0	273.5665414	-17.9228278	1.80	1.36	49.00	35.17 ± 0.02	+0.67
40.0	273.5457926	-17.9284661	2.12	1.76	40.00	37.35 ± 0.03	+0.21
41.0	273.5662283	-17.9256745	1.69	1.47	48.00	35.02 ± 0.06	+0.02
42.0	273.5648070	-17.9262439	2.01	1.65	97.00	36.06 ± 0.06	+1.79
45.0	273.5557839	-17.9182388	2.75	2.44	7.000	35.86 ± 0.12	+0.49
46.0	273.5579243	-17.9306652	1.83	1.75	44.00	39.70 ± 0.05	+1.71
47.0	273.5479984	-17.9272905	2.22	1.72	43.00	35.97 ± 0.03	+0.08
51.0	273.5458037	-17.9289719	1.75	1.43	77.00	37.23 ± 0.03	+0.43
52.0	273.5503813	-17.9228494	1.60	1.12	67.00	34.41 ± 0.04	-0.09
53.0	273.5463654	-17.9421570	1.84	1.37	33.00	36.48 ± 0.06	+1.28
57.0	273.5614471	-17.9187094	2.34	1.89	61.00	35.70 ± 0.03	-0.39
58.0	273.5595440	-17.9178954	1.59	1.45	158.0	34.19 ± 0.09	-0.23
61.0	273.5475497	-17.9266400	1.69	1.04	59.00	37.89 ± 0.02	+0.70
62.0	273.5533917	-17.9280329	2.13	1.63	94.00	34.05 ± 0.02	-0.27
65.0	273.5597707	-17.9186860	1.70	1.52	51.00	34.87 ± 0.07	-0.35

(1) N_2H^+ velocity center (and associated uncertainties) extracted from the `PySpecKit` line-fitting.
(2) V_{DCN} - $V_{N_2H^+}$, positive and negative symbols indicate if the N_2H^+ velocity is blueshifted or redshifted relative to the DCN core velocities.